IEEE Access
Multidisciplinary ⋮ Rapid Review ⋮ Open Access Journal

Received 10 September 2024, accepted 23 September 2024, date of publication 27 September 2024,
date of current version 15 October 2024.

Digital Object Identifier 10.1109/ACCESS.2024.3469550

RESEARCH ARTICLE

ARDÁN: Automated Reference-Free Defocus Characterization for Automotive Near-Field Cameras

DANIEL JAKAB[1,2], EOIN MARTINO GRUA[1,2], REENU MOHANDAS[1], (Member, IEEE), BRIAN MICHAEL DEEGAN[2,3], (Member, IEEE), ANTHONY SCANLAN[1,2], DARA MOLLOY[3], ENDA WARD[4], AND CIARÁN EISING[1,2], (Senior Member, IEEE)

[1]Department of Electronic and Computer Engineering, University of Limerick, Limerick, V94 T9PX Ireland
[2]Lero the Science Foundation Ireland Research Centre for Software, University of Limerick, Limerick, V94 T9PX Ireland
[3]Department of Electrical and Electronic Engineering, University of Galway, Galway, H91 HX31 Ireland
[4]Valeo Vision Systems, Galway, H54 Y276 Ireland

Corresponding author: Daniel Jakab (daniel.jakab@ul.ie)

This work was supported in part by Lero the Science Foundation Ireland Research Centre for Software under Grant 13/RC/2094_P2, in part by Valeo Vision Systems, and in part by European Regional Development Fund through the Southern & Eastern Regional Operational Programme to Lero—The Science Foundation Ireland Research Centre for Software (www.lero.ie).

ABSTRACT Measuring optical quality in camera lenses is crucial in evaluating cameras, especially for safety-critical visual perception tasks in automotive driving. While ground-truth labels and annotations are provided in publicly available automotive datasets for computer vision tasks, there is a lack of information on the image quality of camera lenses used for data collection. To compensate for this, we propose an Automated Reference-free Defocus characterization for Automotive Near-field cameras (ARDÁN) to evaluate Slanted Edges for ISO12233 in five publicly available automotive datasets using a valid and invalid region of interest (ROI) selection system in natural scenes. We use the mean of 50% of the Modulation Transfer Function (MTF50) in three Camera Radii (CaRa) segments and the Overall Spread in Heatmaps (O'SHea) for an 8×5 distribution to evaluate the quality of edges in natural scenes. From the experiments performed, lenses with uniform spatial domains (i.e. little distortion) showed that MTF50 was constant between (0.18-0.25cy/px). With image rectification on the same scenes, MTF50 results artificially increased, no longer representing the camera lens. In contrast, for strong radial distortion, MTF50 varied extensively across the spatial domain between (0.12-0.4cy/px), where, in particular, Woodscape gave the highest average of MTF50 per region for natural scenes.

INDEX TERMS Automotive, camera radii (CaRa), energy inspection limit above Nyquist (EiLíN), natural scenes, optical quality, the overall spread in heatmaps (O'SHea), radial distortion, regional mask to lens alignment (RMLA), slanted edges, valid and invalid region of interest (ROI) selection system.

I. INTRODUCTION

Measuring optical quality in camera lenses has traditionally been restricted to laboratory conditions [1]. Laboratory conditions involve specialized test charts explicitly designed for the type of lens used in measurements. It is much more challenging to measure the optical quality of wide field-of-view (FOV) cameras mainly because specialized test charts and laboratory settings need to be designed depending on the degree of FOV, which can be anywhere between 60°-190° for fisheye cameras. For an automotive setup, four 190° cameras have been proven to work to capture the surround-view of a typical five-seater vehicle [2].

Automotive camera datasets generally do not have the optical properties measured before the release of the dataset, which is crucial information in determining which data to

The associate editor coordinating the review of this manuscript and approving it for publication was Shadi Alawneh.

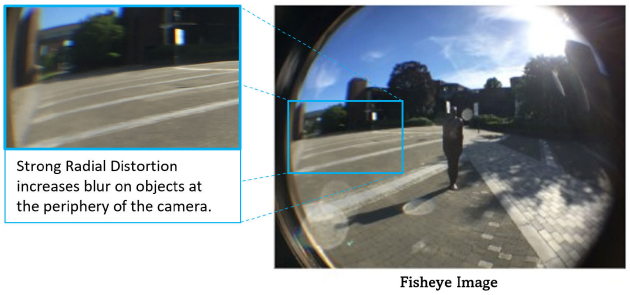

FIGURE 1. Strong Radial Distortion affecting Image Quality. Notice how the left side of the bounding box(blue) has visually lower quality than the right side where image scenery moves from the center to the periphery of the camera (see further optical artifacts evident in this scene in Jakab et al. [9]).

use for computer vision. Additionally, it is unrealistic to expect the optical quality of cameras to stay consistent with laboratory production tests, as cameras can change with time due to consistent usage and external factors such as varying temperatures in the natural environment. Therefore, cameras in an automotive scenario can vary in terms of optical quality and can inadvertently impact automotive perception. It has been shown in previous work that external factors such as windshields placed in front of automotive cameras [3], [4], the varying geometric properties of camera lenses [5], [6] and the robustness to realistic optical aberrations [7] can directly impact image quality and in turn the computer vision performance on the road.

It has been investigated for quite some time how image and optical quality impact computer vision and perception performance [8], [9]. However, in many circumstances, the optical quality of a system is unknown. For example, public datasets do not typically provide optical quality information, as they have not been measured in laboratory experiments. In this study, we intend to investigate and measure camera quality from natural scenes and simulation, especially for fisheye cameras with strong radial distortion. It is essential to know how the details captured through a camera are impacted as if they were deployed directly in the automotive environment. By obtaining measurement results, we aim to bridge the gap in knowledge for public datasets in terms of optical quality assessment and enable researchers to account for the optical quality in the data when using computer vision or perception systems in self-driving cars.

If the real-time evaluation of cameras is possible in natural scenes, and the optical quality of cameras can be continuously measured, we have the potential for increased road safety and better quality automotive perception on the road.

There has been little research on how automotive cameras could degrade further in optical quality once deployed in the environment and can have an inherent effect on computer vision algorithms. Unlike standard Digital single-lens reflex(DSLR) and typical smartphone cameras (which were the basis of experiments for Zwanenberg et al. [10], [11]), automotive fisheye cameras have strong radial distortion at the periphery of the image and other optical artifacts such as vignetting which can be seen due to the camera optical system or a camera and imaging sensor mismatch [9]. A real-time camera monitoring system would provide the user with information on when to replace degraded automotive cameras should a drastic change in camera behavior occur. Having high-quality cameras for automotive driving tasks is important, considering that computer vision models depend on high-quality perception.

Zwanenberg et al. proposed Natural Scenes Spatial Frequency Response (NS-SFR) [10], [11], [12], [13], [14] which measures slanted edges in natural scenes to estimate the image quality of lenses utilizing BSISO12233:2017 [15] Slanted Edge algorithm originally developed by Burns et al. [16]. Zwanenberg's experiments were centered around DSLR and smartphone cameras with a narrow FOV [12].

The initial work of ARDÁN was presented previously in conference proceedings [17]. In this paper, we extend this initial work as follows:

1) Introduce the alignment of regional masks in datasets, which improves the application of masks on any dataset.
2) Examining both rectified and unrectified images of the same natural scene in the KITTI [18] dataset where geometric distortion is removed in the rectified images, investigating its impact on measurements.
3) Examining a wide range of different camera perspectives for automotive cameras where cameras can be mounted on top of the vehicle(e.g., see datasets KITTI [18] and KITTI-360 [19]) or close to the ground, typically associated with fisheye datasets (e.g., see all four camera perspectives for Woodscape [20].
4) Introducing slope monitoring and energy measurement above Nyquist to investigate and enhance slanted edge selection in automotive scenes.
5) Performing a rigorous region-by-region image sharpness analysis in heatmaps.
6) Updating from the ISO12233:2017 standard to the ISO12233:2023 standard using default settings, which now corrects for non-uniformity and angle-based correction to account for both geometric distortion and vignetting effects found in cameras.

In this paper, our contributions are as follows:

- We propose **Regional Mask to Lens Alignment (RMLA)** to remove ego-vehicle occlusion and mechanical and optical vignetting [9],
- We introduce a **Valid and Invalid Region of Interest (ROI) Selection System** to evaluate five automotive datasets where all camera perspectives are tested separately for ISO12233:2023 [21],
- We introduce **Camera Radii (CaRa)** to investigate the strong radial distortion from the center to the periphery of fisheye cameras,
- We propose the **Overall Spread in Heatmaps (O'SHea)** technique to examine region by region results

for optical quality in a 8×5 (explained in Section III-H) heatmap segmentation of images in datasets,

- We investigate the use of constraint techniques such as monitoring the **Slope of the Modulation Transfer Function (Slo-MTF)** and introducing an **Energy Inspection Limit above Nyquist (EiLíN)** to examine region-by-region of results for optical quality in a 8×5 rectangular segmentation of dataset images,

Our experiments use five datasets where, four are real-life datasets with 90° (KITTI) [18], 180° (KITTI-360) [19], 185° (LMS) [22] and 190° (Woodscape) [20] FOV respectively. The 5th dataset (SynWoodscape) [23] is a CARLA simulation [24] which incorporates the 190° FOV of the 4th dataset.

The experiments outlined here address the gap in the literature to evaluate public datasets for image quality where the perceived sharpness or edge contrast as seen through cameras is measured when deployed in the automotive environment. A pipeline to evaluate multiple datasets using a controlled strategy for measurement, applying constraints to slanted edge selection, and producing both qualitative and quantitative analyses for evaluation, is developed.

We hope other researchers will find our methods for establishing optical quality measurements in natural scenes useful. Our code is available at https://github.com/danieleceUL/ARDAN.

In the following sections of this paper, we will discuss Related Works in Section II, Methodology in Section III, Datasets in Section IV, Results in Section V, Limitations with Future Work in Section VI, and the Conclusion in Section VII.

II. RELATED WORK

Assessing the optical quality of cameras has been a crucial part of the computer vision deployment process regardless of application. For cameras to be of reasonable quality, the components must undergo production tests individually and during assembly. In most cases, tests are performed repetitively throughout the pipeline to ensure that optical quality is retained after each assembly step. The industry sets tolerance limits for the mass production of cameras. One challenge in deploying cameras is monitoring camera systems' inherent aging and environmental influences in real-time. The combination of mass production and optical quality tests for computer vision should be established [25].

The typical image quality measurement is the process of measuring the camera's sharpness, and a measurement test chart is used to produce test images. Typically, slanted edges are a proven and universally accepted method of measurement where edges that transition from dark to white pixels or vice versa are measured through the camera's lens [21]. There have been several improvements in measuring optical performance for slanted edges, such as the polynomial edge fitting added to the slanted edge technique in the fourth version of the algorithm [16]. Sfrmat4 is a Matlab software script function (see the Burns Digital Imaging website [26] for more information), which provides a Spatial Frequency Response (SFR) from digital image files using the Slanted Edge Method. It follows the ISO12233 standard [15], developed by the Technical Committee ISI/TC 42 to resolve photographic cameras' measurements [27]. The ISO12233:2023 [21] version of the Slanted Edge Method has replaced the fourth version of ISO12233:2017 [15] (sfrmat4), which now provides polynomial edge fitting to curved edges. The polynomial edge fitting optimization compensates for the fact that slanted edges are not always a straight line in practice. Sfrmat5 [21] provides experiments with advanced edge fitting, a comparison with two smoothing windows called Tukey and Hamming, as well as the correction for non-uniformity in images [28]. The Slanted Edge Method, as detailed in the latest standard [21], isolates a bounding box region from a photographed image where there is a clear grayscale transition between dark to white pixels tilted at an angle which forms a slanted edge [10, p. 22].

In recent years, optical quality experiments have transitioned to measuring camera imagery outside laboratory conditions [29], [30]. Zwanenberg et al. [10], [11], [12], [13] proposes the latest such pipeline where edges were extracted from natural scenes using canny edge detection and masking to optimize natural scene measurements using the fourth version of the Slanted Edge Method (sfrmat4) [15]. This work [10], implemented a large-scale version of the Slanted Edge Method [15] in linearized natural scenes wherein slanted edges were found and extracted for measurement called the Natural Scenes Spatial Frequency Response(NS-SFR) technique. The Slanted Edge Method [15] is applied to each extracted edge within the natural scene. This edge extraction can be repeated across a dataset of images to obtain a strong pattern of measurements independent of the scene. A brief outline of the original NS-SFR framework is as follows [11, pp. 55-57]:

1) An image dataset originating from the same camera system must be provided as an input where each image is selected at a time for processing.
2) Each image is rotated by 90° (i.e. for vertical edges), linearized using Adobe RGB [31] or sRGB [32] linearization and normalized for image processing.
3) Edges are detected using the Canny edge detector adapted to the previous step's vertical and horizontal edge orientations.
4) A proximity filter is applied to horizontal and vertical images to remove edges within five pixels of the neighboring edge.
5) Edge locations are passed through ROI selection, which crops ROI windows from the linearized image. An edge isolation filter separates the edge of interest from unwanted artifacts, such as other edges or scene textures (also known as pixel-stretching).
6) The isolated edges are examined and filtered to ensure uniformity on either side of the edges.
7) Finally, the edges are processed using the Slanted Edge Method(sfrmat4) [15], producing a series of NS-SFRs for each image.

8) By iterating over the entire image dataset, an overall picture can be obtained about the optical quality of the camera used for the dataset.

In earlier work, Zwanenberg et al. [13] investigated the procedure of extracting edges from pictorial natural scenes using different edge detection methods where the Canny edge detection filter produced the most suitable measurements in terms of Signal-to-Noise Ratio (SNR) [33]. The suitability of the edge detection filters was evaluated by applying different variations of Gaussian white noise to a test image and extracting edges from it using the NS-SFR framework specified above. The degree of Gaussian white noise applied to the slanted edge (measured in SNR) showed that at around 14dB (i.e., a ratio of 5:1) or higher ratios, the Canny edge detection filter was much more efficient than the feature-matched filter (i.e., the second edge detection filter compared in this work) [13]. The latest work by Zwanenberg et al. [12] improves the computational time of the framework by up to (22x) faster than the original. Furthermore, the pixel-stretching technique used in the original NS-SFR framework for the slanted edge regions was replaced by edge masking, which produced computationally optimized results.

From the measurements of slanted edges, the Spatial Frequency Response (SFR) otherwise known as the Modulation Transfer Function(MTF) can be obtained which indicates the sharpness of the camera and is a spatial resolution measurement. The MTF curve varies with optical and imaging system performance as described by Zwanenberg et al. [10, pp. 1-2]. A typical measurement for cameras would be measuring 50% of the MTF curve, otherwise known as MTF50, which is a measurement of sharpness [10, p. 36-37]. MTF50 is a measure of image sharpness, where an unsharpened camera system would produce a low MTF50 score and a highly sharpened camera system with a high MTF50 score.

The above studies into the NS-SFR pipeline are significant, as they provide a robust approach to measuring optical quality directly from natural scenes. However, from the studies performed, there has been no investigation or measurement of NS-SFR with fisheye lenses, which have inherently strong radial distortions. Fisheye optics vary significantly due to its spatially variant optical properties. For example, a single MTF50 score for a fisheye camera at the center of the lens is different for the periphery of the same camera. Obtaining regional scores would be a more effective strategy in measuring such distortions. Currently, a strategy for fisheye cameras is to devise a measurement test chart to the particular degree of FOV measuring against strong radial distortion (see [1] for more information on pre-distorted test charts). Due to the additional feature of the slanted edge measurement, polynomial edge fitting, edges are no longer required to be a perfect straight line. In 2020, Burns et al. [34] showed the inherent effect of circular slanted edges where a curved test chart directly affected image quality measurements. In these cases, it is reasonable to assume that the inherent circular nature of fisheye cameras will influence image quality measurements spatially. This is because curved edges can now be measured with the NS-SFR framework, and curved edges are much more apparent in fisheye imagery than in typical rectilinear or pinhole cameras.

Finally, an issue we address is the evaluation of automotive camera image simulations, especially fisheye simulations. As of the writing of this study, little to no research has been performed in this area. To ensure the simulations we use for training data in computer vision algorithms are of reasonable quality, we measure the optical quality of the simulation and establish a set of standards for simulation to produce synthetic data of sufficient quality for self-driving training. Reliability and safety are paramount when utilizing synthetic data for autonomous driving. A framework recently proposed by Mueller et al. [35] has been developed to assess the differences between real-life and synthetic images. This framework can evaluate synthetic data rendered from a graphics engine with a virtual camera model or taken by a high-quality Digital Single-Lens Reflex (DSLR) camera using the ISO12233:2017 [15] standard. From the results in [35], it was found that the Zernike model (which can be analytically described by Zernike polynomials [36]) most closely modeled the real-life lens from the laboratory indicating that this framework can potentially serve as a benchmark for future simulation evaluations. ARDÁN, the proposed platform of this study, aims to address the research gaps identified above by reusing the optimized NS-SFR pipeline [12] for all experiments where the optimized method is refined to use the ISO12233:2023 standard to measure slanted edges in automotive datasets.

III. METHODOLOGY

These experiments aim to extract a set of edges from a dataset that can be used subsequently to estimate the spatial frequency response, which, in turn, is the camera's image quality. The pipeline for experiments can be seen in Figure 2. Each dataset contains one particular type of camera capturing a set of dynamic frames of a natural scene. Once appropriate edges are extracted, the measurements are performed on each ROI, and the image quality for each edge is estimated for each given edge. The edge locations are then categorized into three radial distances aligned with the camera aperture. The edge locations are also separately categorized into 8×5 regions where the edge locations are grouped according to the respective pixel coordinates. Finally, the mean Slanted Edge-based Spatial Frequency Response(e-SFR) is calculated for each radial distance and region. The final results are then visualized. The values obtained from both strategies will provide insight into the image quality pattern for each particular camera used. The constraints from previous work [17] were initially chosen to reduce and isolate good measurements for slanted edges in natural scenes, which can be very noisy above Nyquist, where different textures, shapes, and or components can be found. Lighting conditions and external factors in the environment can also affect image quality. The recommended

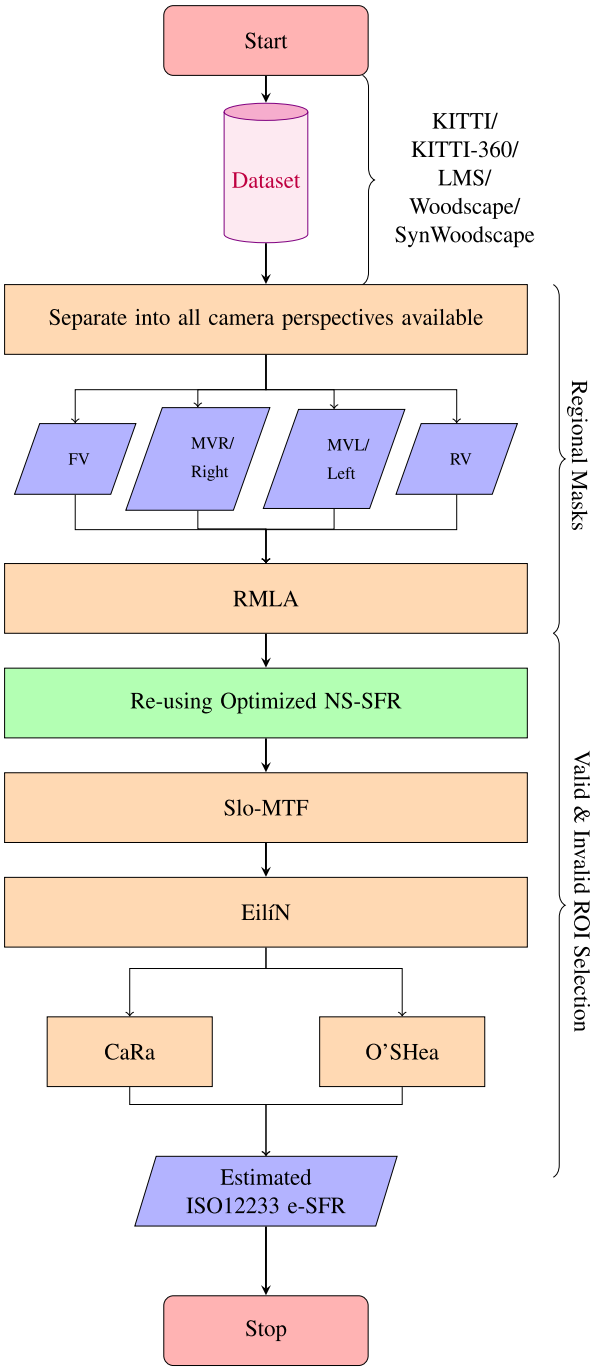

FIGURE 2. The ARDÁN Pipeline. Each camera perspective of a dataset should apply regional masks, use optimized NS-SFR, apply regional selection constraints (i.e., Slo-MTF, EiLiN), and finally, relevant analyses for camera evaluation (i.e., CaRa, O'SHea).

guidelines for acceptable edges can be found on the Imatest website(see [37] for information on Modulation Transfer Function (MTF) curves and Image appearance). For example, in datasets such as Woodscape, there was a strong presence of edge enhancement and noise or aliasing in the measurements of the ROI Selection. The minima constraint from current work (as depicted in Figure 3) might not be sufficient in

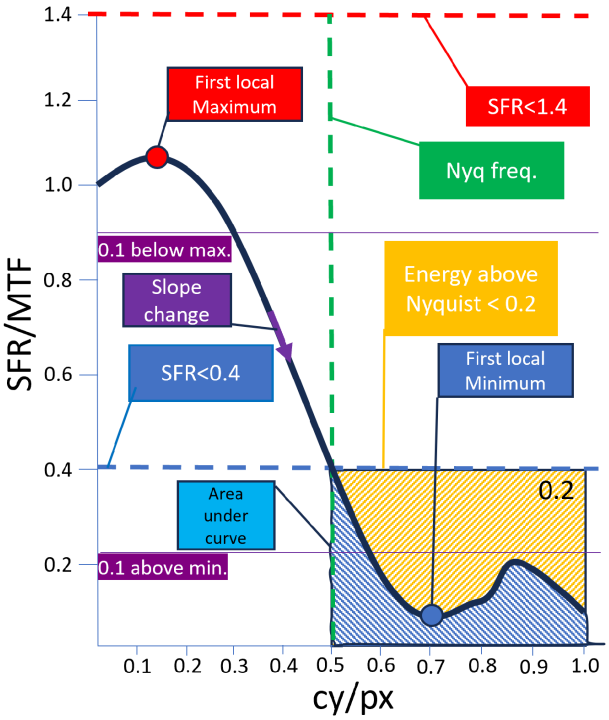

FIGURE 3. Diagram of MTF constraints. Note: all slope changes are checked at an offset of 0.1 from both local maximum and minimum locations. This is partly due to the low probability of finding a large slope change within proximity of these locations.

measurements where local minima can exceed the 0.4 SFR threshold but can still be classified as a good measurement. Overall, this strategy minimizes large peaks in measurements and reduces wavy field curvature measurements or large astigmatism from affecting results.

The methodology for experimental analysis is shown in Figure 2 where the measurement pipeline can be broken down into the following components: Regional Masks in Section III-A, Regional Mask to Lens Alignment (RMLA) in Section III-B, Reusing Optimized NS-SFR in Section III-C, Slope of Modulation Transfer Function (Slo-MTF) in Section III-D, the Energy Inspection Limit above Nyquist (EiLiN) in Section III-E, Valid and Invalid ROI Selection in Section III-F, Camera Radii(CaRa) in Section III-G and the Overall Spread in Heatmaps(O'SHea) in Section III-H,.

A. REGIONAL MASKS

Regional Masks are masks applied to images isolating a region to perform optical quality measurements. This region is otherwise known as the natural scene taken by the camera. This is important, especially in fisheye cameras where ego-vehicle occlusion and camera vignetting partially obstruct the camera's field of view. For example, the Woodscape dataset (a typical automotive fisheye dataset) contains four views, all containing camera vignetting and ego-vehicle occlusion in the images. Therefore, as illustrated in Figures 4a-4d, a regional mask is defined and applied for each image

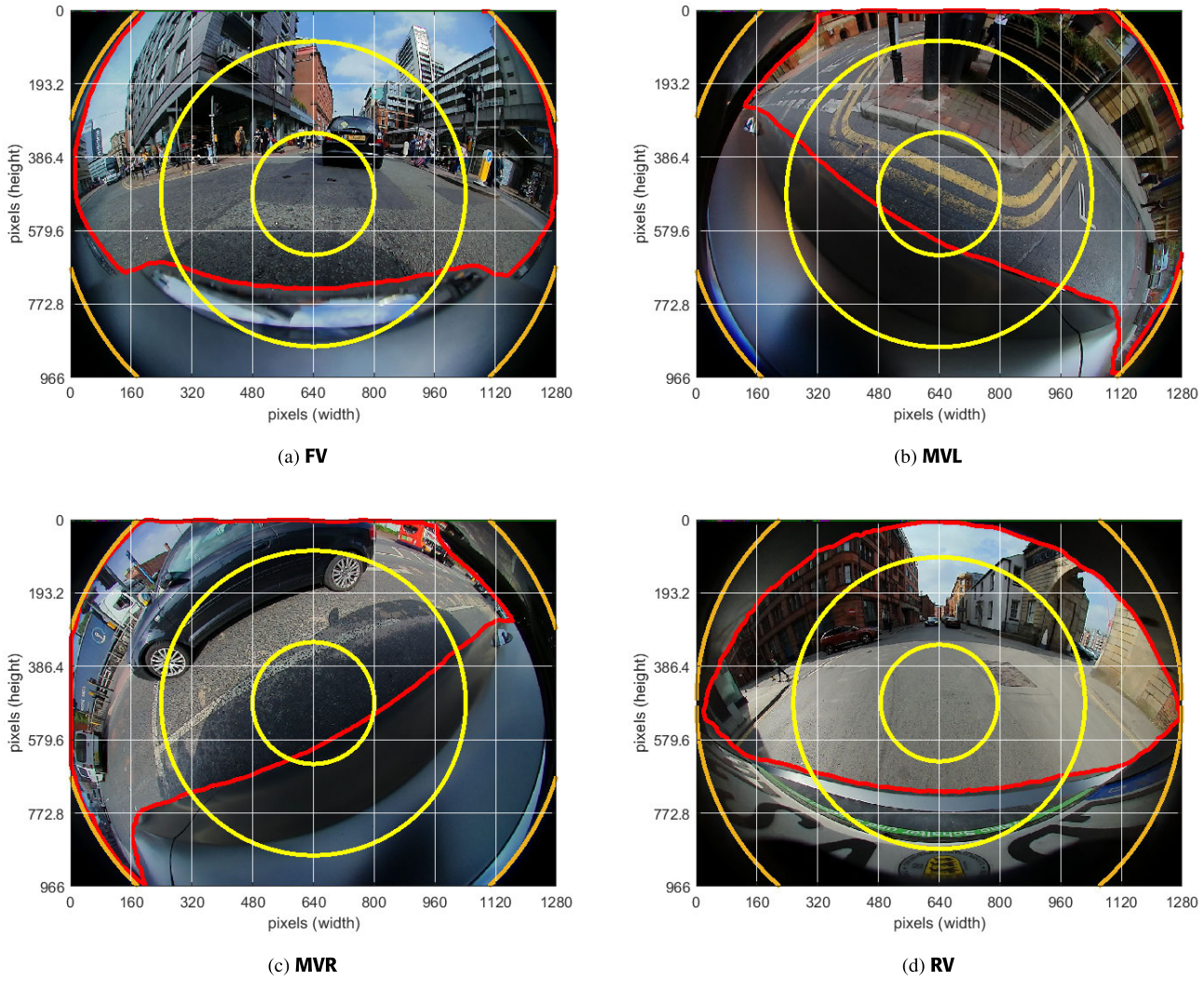

(a) **FV** (b) **MVL**

(c) **MVR** (d) **RV**

FIGURE 4. RMLA and CaRa on all four perspectives of Woodscape. Note: Inner (yellow) and outer (orange) CaRa, RMLA(red), and 8 × 5 Heatmap spatial domain(white grid) for FV Woodscape. CaRa are aligned with the periphery of the fisheye camera, and any edge categorized represents the lens location.

isolating the natural scene; these Regional Masks are created manually but may be automated [38]. All regional masks are created using the Freehand ROI tool from MATLAB [39] allowing the user to customize a particular ROI mask to isolate the natural scene. A new mask is created if a new camera fits the scene.

B. REGIONAL MASK TO LENS ALIGNMENT (RMLA)

With the addition of Regional Mask Lens Alignment, there would be uniform measurements obeying the geometry of the natural scene and the camera's aperture regardless of the perspective (especially in wide FOV images such as Woodscape, which is difficult to avoid). The implementation of Regional Masks and CaRa are generalized for surround-view perspectives, such as Woodscape, as seen in Figure 4.

C. RE-USE OPTIMIZED NS-SFR

The ROI selection technique and parameter tuning of the NS-SFR optimized algorithm [12] is reused here. Canny Edge Detection with edge masking is used to find edges from the natural scenes and isolate edges of interest. The NS-SFR parameters that determine slanted edge selection in natural scenes are the following:

1) **Contrast Range** (0.1 - 0.9) - the contrast range between the transition from dark to white in a region with a slanted edge:
   a) Low contrast (<0.1) is prone to noise error,
   b) High contrast (>0.9) is prone to non-linear sharpening and image processing,
2) **Edge Angle Range** (0° - 360°) - there is no restriction on the angle range of slanted edges as it limits the number of edges that can be found in a natural scene

except for 0° and 45° which are filtered out and is not possible due to errors [15],

3) **Step Edge Noise Floor (ST)** (0.02) ensures that the gradient on either side of the edge is uniform. For example, a value of 0.02 signifies a change of pixel value or digital number (DN) of 4.5 for an 8-bit image [11],
4) **Edge Spread Function Width (esfW)** (default value is 5 pixels) remove edges too close together. For example, edges can be 5 pixels apart in an image,

As a basis for a complete and controlled analysis, the default parameters originally proposed by Zwanenberg et al. were used [11] (i.e., ST=0.02, esfW=5 pixels). This was done to understand what happens if distortion is applied to the images and whether a consistent pattern can be observed across the datasets.

D. SLOPE OF MODULATION TRANSFER FUNCTION (SLO-MTF)

The Slope of Modulation Transfer Function (Slo-MTF), otherwise known as the rate of change of MTF, is an important factor to consider when evaluating the quality of slanted edges. A typical MTF has a smooth descending curve, as seen in Figure 3. For an MTF function, a negative slope signifies the transition from white to black pixels or visa-versa from a smooth edge spread function. Therefore, it is important to investigate the slope change of MTF curves and to ensure that the transition is relatively smooth to ensure a monotonically descending slope (i.e., the slope must always be <0). A check for slope change is added to constraints (see Figure 5 for sample results). In this work, we introduce this slope check between the first local maximum and minimum measurements, where the most significant drop in MTF across the sampling points is. This is mostly between the range of 0 and 1. If no edge enhancements exist in MTF measurements, the first local maximum is taken where a magnitude of 1 is expected (otherwise, the maximum MTF peak can be 1.4). Slope change is monitored until the first local minimum, As shown in Figure 3, the purple arrow between both purple horizontal limits indicates a check for slope change between the first local maximum and above the first local minimum. The slope should be monotonically descending. This approach removes unsmooth slope measurements such as the light green line from Figure 5c in ROI selection corresponding to Figure 5a, thus improving the quality of data being collected. The following results are from experiments using the 2023 version of the slanted edge algorithm [21].

E. ENERGY INSPECTION LIMIT ABOVE NYQUIST (EILÍN)

An additional feature of the proposed method is providing a limit to energy past the Nyquist Frequency, which is MTF above 0.5 cy/px. An ideal slanted edge should have minimal energy past this point, where high energy may indicate aliasing in slanted edge measurements. Having high energy past Nyquist while arguably not a definitive indicator of aliasing [40], discarding these measurements, removes the possibility of aliasing being an issue in this context where an over-estimation of MTF50 measurements can occur. This is especially important since all measurements are in a highly unpredictable and dynamic environment, which is the definition of the natural scene. As a strategy to address over-estimation, we utilize the local minima constraint of 0.4 SFR (introduced previously in Section III-F) where the MTF area should not exceed the area under this constraint, which is 0.2 ($0.5cy/px \times 0.4SFR$).

F. VALID & INVALID ROI SELECTION

We apply the following constraints to slanted edge selection:

1) **Local Maxima $<$ 1.4 SFR** - If local maxima exceed a peak of 1.4 SFR ($\cong$ 25% overshoot), the measurement is discarded. 25% overshoot or less is acceptable [37] for slanted edges,
2) **Local Minima $<$ 0.4 SFR** - If the local minima exceed 0.4 SFR, the measurement is discarded. A low threshold of <0.4SFR will filter out signals with excessive noise past the Nyquist frequency (0.5cy/px) [13],

Measurements that meet the above requirements are marked by a green bounding box, and those that do not are marked by a red bounding box (see Figure 5). Invalid edges with strong edge enhancement, noise artifacts, or invalid measurements are labeled as red bounding boxes. Edge enhancement is a typical artifact found in image quality measurements with a slight rise and fall at the beginning (usually between 0-0.3 cy/pixel) of the MTF signal. Excessive edge enhancement (i.e., a peak MTF value greater than 1.4) is undesired mainly because it affects the degree of image quality measurements obtainable from the slanted edge. Noise in slanted edges is also problematic, causing aliasing or false artifacts to appear in measurements. Measurements disproportionately affected by these artifacts are discarded from the results. Green bounding boxes represent valid ROIs resembling quality slanted edges with few artifacts.

G. CAMERA RADII (CaRa)

To analyze the images further, three Camera Radii(CaRas) will categorize the location of each slanted edge according to its relative distance from the center of the image. The basis of this is the expectation that the optical effects of the lens will be (at least approximately) radially symmetric. The technique used to create each segment is by taking the Euclidean distance from the central point to the farthest edge of the Regional mask. In the case of KITTI, the corner of the image was taken as the farthest distance from the center of the image, as no mask is defined. The following formula represents the Euclidean distance calculation:

$$r_e = \max\left(\sqrt{(x_c - x_m)^2 + (y_c - y_m)^2}\right) \forall (x_m, y_m) \in [X_m, Y_m] \tag{1}$$

where r_e is the Euclidean distance representing the radius of the largest radial distance (i.e., the orange circles (please

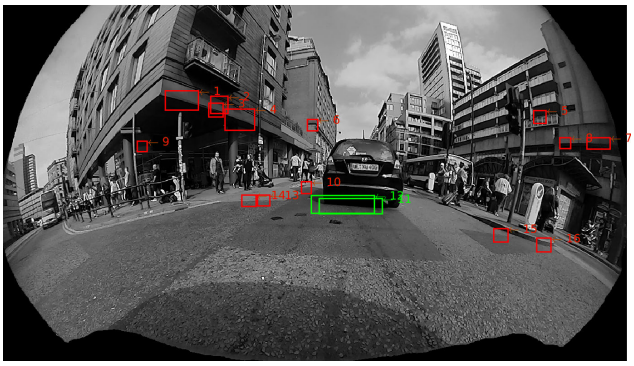

(a) **Original Woodscape**

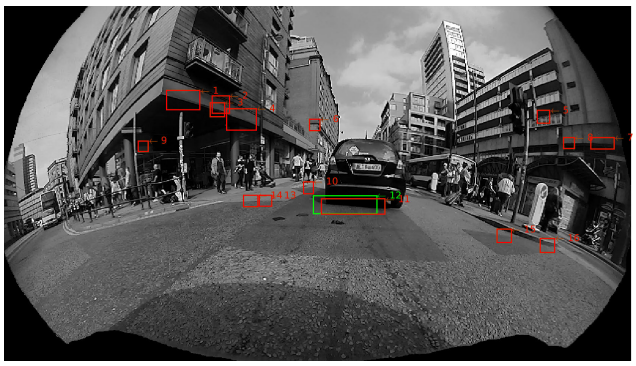

(b) **Slo-MTF Woodscape**

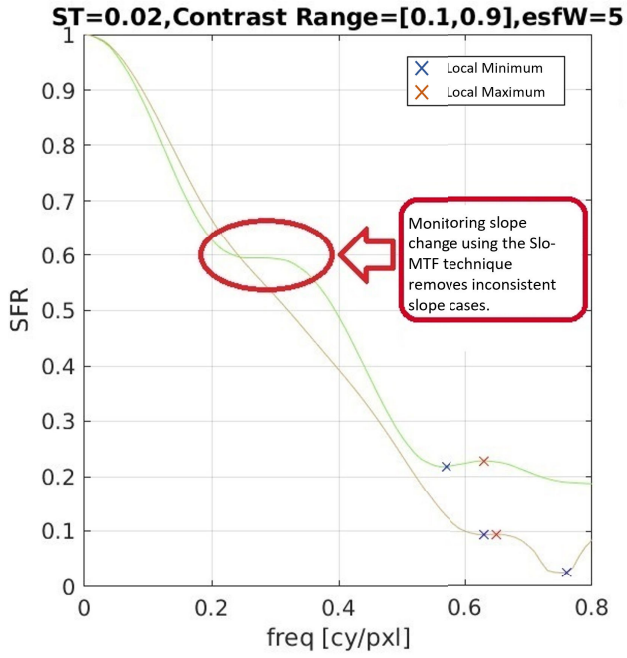

(c) **Original Woodscape**

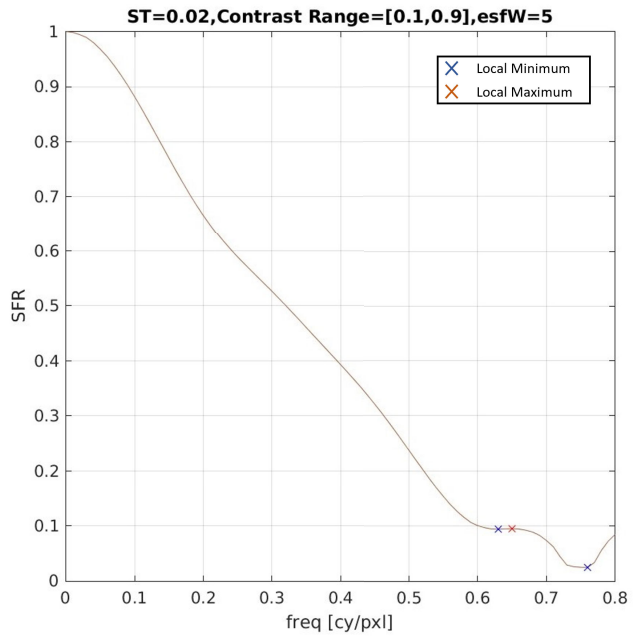

(d) **Slo-MTF Woodscape**

FIGURE 5. **A demonstration of filtering out MTF measurements that have an inconsistent positive or negative (+/−) slope change using the Slo-MTF technique. Slo-MTF is applied between the first local maximum (a value of *SFR* = 1 in both cases) and the first local minimum (a blue x symbol) along each MTF curve for ISO12233:2023 [21]. (a) and (b) show the ROI selection of horizontal slanted edges in the natural scene of FV Woodscape before and after Slo-MTF is applied. (c) and (d) show MTF measurements on FV Woodscape before and after Slo-MTF is applied.**

see Figure 4 as an example of CaRa on Woodscape) except for KITTI where the orange circle is not visible due to the radius being the distance from the corner to the center of the image [17]), the point (x_c, y_c) represent the location of the center of the image or mask, (x_m, y_m) represent points along the periphery of the Regional mask $[X_m, Y_m]$ (see red outline of RMLA in Figure 4) and can be the location of the bottom right corner of the image if no mask is present. (Note: If no ROI is set, $[X_m, Y_m]$ is the periphery of the image). The radii of CaRA are obtained by dividing the maximum radius r_e into N proportional parts. The ratios determined in these calculations are suitable mainly because they give sufficient segments to divide the images into three categories (i.e., center, middle, and edge) and generalize well regardless of camera type. Ratios smaller than this are unsuitable (i.e., there tends to be bias towards having too many slanted edges favored for one segment).

H. OVERALL SPREAD IN HEATMAPS (O'SHea)

In addition to CaRa, we introduce Overall Spread in Heatmaps (O'SHea) as a method for a more rigorous optical quality evaluation. Typically, image sensors are rectangularly aligned to the lens of the camera, where the horizontal and vertical sizes of the image produced have a given ratio or resolution. Many standard camera resolutions are available that can be translated to screen resolution sizes of 720p or High Definition, 1080p (Full HD), 1440p (2k), and so on, which would all be compatible with typical television or

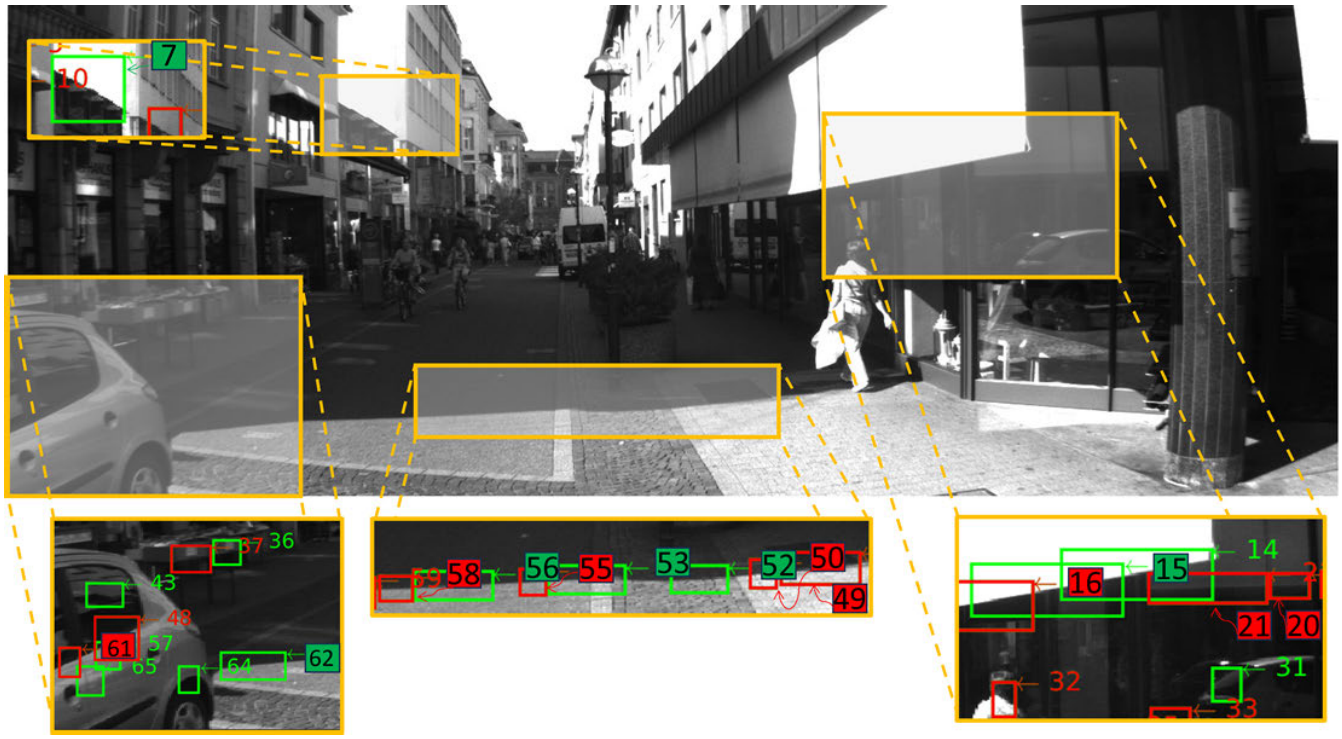

FIGURE 6. Qualitative results for Unrectified KITTI horizontal slanted edges.

display screens. The standard HD resolution ratio, which is 1280×720 pixels, is approximately 1.78:1, and if examining larger resolutions, this ratio remains constant. We choose a heatmap ratio, which would approximate the resolution ratio without exceeding it, where dividing images by 8×5 would result in an equivalent ratio of 1.6:1.

IV. DATASETS

To do a comprehensive set of experiments in this study, we use a diverse set of data that has variations in radial distortion, varying degrees of FOV, and varying camera positions in natural scenes. We also wish to demonstrate that the proposed method can produce results that have already been achieved in previous work [10], [12]. The KITTI dataset is an ideal candidate for comparison with previous work [17] where images contain minimal distortion (see Figure 6 for sample results of KITTI unrectified qualitative results)for a narrow FOV camera. KITTI is a proven and tested dataset for the automotive driving scenario in training and testing computer vision algorithms [18]. In addition, there are synchronized and processed versions of the KITTI dataset where the distortion has been removed from the images (see Figure 7 for rectified KITTI qualitative results). Undistortion is a common means to force images to adhere to the pinhole projection model, which simplifies the camera model [41]. However, undistortion requires interpolation of pixel values, which can impact the apparent optical quality. Therefore, additional experiments for the same natural scene with and without distortion would be of great interest in experiments.

Of course, our focus is on extending the functionality of the NS-SFR algorithm to automotive near-field/fisheye cameras. Thus, we also select a set of automotive datasets where the fisheye camera is positioned in a surround-view configuration. For example, the Woodscape dataset [20] contains four different viewpoints of surround view, and the camera system is built for low-speed maneuvering and automated parking. KITTI-360 [19] is a second surround-view fisheye dataset that has two cameras positioned on top of a vehicle at 180° to each other. In comparison to Woodscape, the KITTI-360 natural scene has a greater visibility of the nearby buildings beside the road than the mirror views of Woodscape due to the added height of the camera position. Hence, both datasets provide a diverse set of experiments for the fisheye camera. In both fisheye datasets, ego-vehicle occlusion is present in all images. These regions are not part of the natural scene and must be removed by a custom regional mask using RMLA to avoid biasing the results. In contrast to the Woodscape [20] and KITTI [19] fisheye datasets, the LMS dataset [22] consists of a circular fisheye camera with no ego-vehicle occlusion. In addition, LMS has provided a checkerboard calibration test chart in laboratory conditions, which is useful for measuring slanted edges equivalent to those found in natural scenes. Finally, a synthetic fisheye dataset is required to compare the simulation to real-life optical quality. As a result, the SynWoodscape dataset [23] can be considered where the intrinsic calibration model of Woodscape is applied to the simulation.

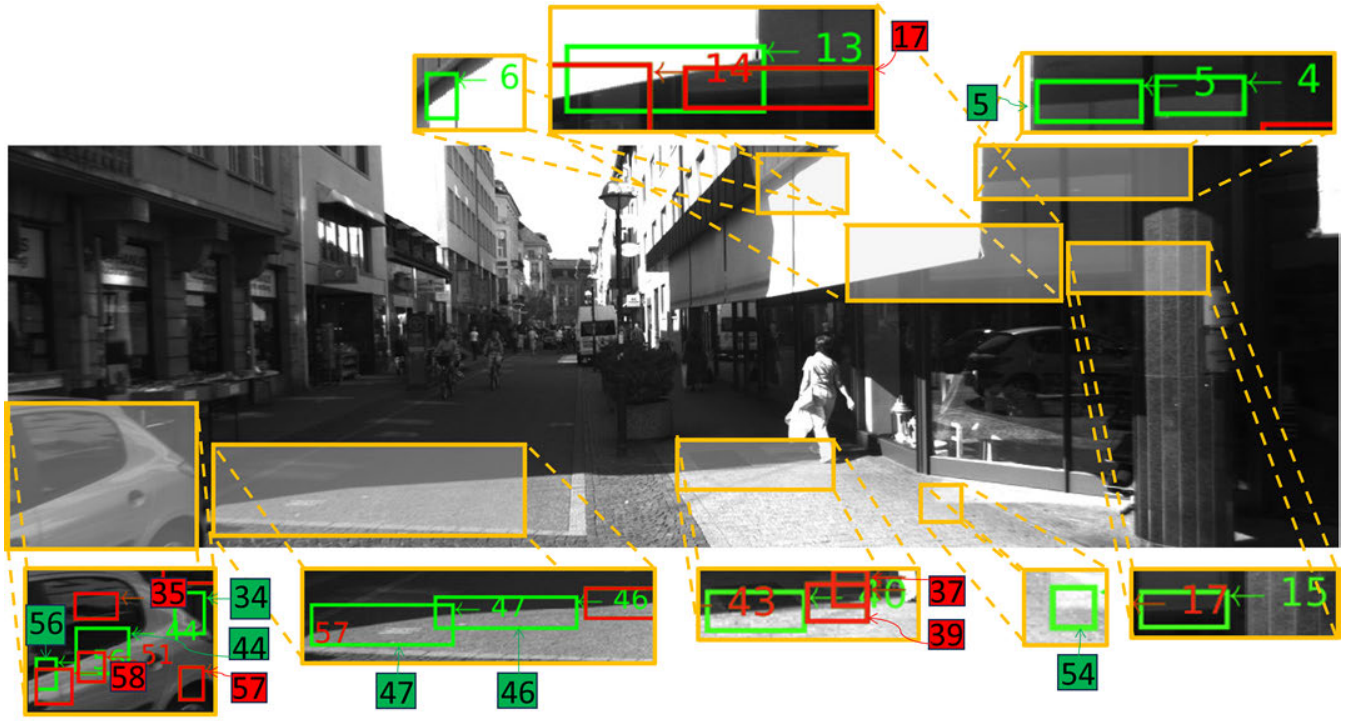

FIGURE 7. Qualitative results for Rectified KITTI for horizontal slanted edges.

TABLE 1. Automotive datasets used in experiments.

Dataset	No. Images	FOV	FV	MVL	MVR	RV	Left	Right	No. cameras
KITTI	1065	90	✓	X	X	X	X	X	4: (2x) gray, (2x) colored
KITTI*	1059	90	✓	X	X	X	X	X	4: (2x) gray, (2x) colored
KITTI-360	Left (11518), Right (11519)	180	X	X	X	X	✓	✓	2: (1x) left, (1x) right
LMS	1251	185	X	X	X	✓	X	X	1
LMS Calibration	39	185	X	X	X	✓	X	X	1
Woodscape	1514 (FV), 2054(MVL), 1511(MVR), 1512(RV)	190	✓	✓	✓	✓	X	X	4
SynWoodscape	500 (FV), 500(MVL), 500(MVR), 500(RV)	190	✓	✓	✓	✓	X	X	4

* Rectified and synchronized KITTI where distortion is removed from the original images. Note: for synchronization, the first five images are removed from the original data.

The list of datasets used in this study is shown in Table 1. Six possible camera perspectives are listed in the datasets. The experiments conducted in this work divide the datasets up into their respective perspectives as shown in the ARDÁN pipeline 2:

1) Front View (FV)
2) Mirror View Left (MVL)
3) Mirror View Right (MVR)
4) Rear View (RV)
5) Left[1]
6) Right[1]

Each dataset has one lens calibration and a customized regional mask except KITTI which does not have any ego-body occlusion hence, no mask was needed [17].

[1]Note: the final two camera perspectives are referred to as general left and right for KITTI-360 concerning the ego-vehicle position where the camera is on top of the vehicle not at the wing mirror as is the case for the Woodscape perspectives.

V. RESULTS

This section presents the results from the datasets outlined in Section IV. We will first outline how each dataset will be used in experiments. As a basis for performance comparison, we will investigate how the proposed method behaves with the KITTI dataset as a suitable benchmark for experiments. Two versions of the same scene are used as a basis for experiments, as shown in Table 1 where one is unrectified, and the other is rectified (distortion is removed). We will then experiment on datasets with wide FOV (i.e., 180°+), which have strong radial distortion at the periphery of the natural scenes. Both horizontal and vertical edges are shown in experiments.

A. KITTI

In this section, we will present an example of a KITTI ROI selection of a natural scene using NS-SFR with edge masking as a basis for identifying slanted edges in natural

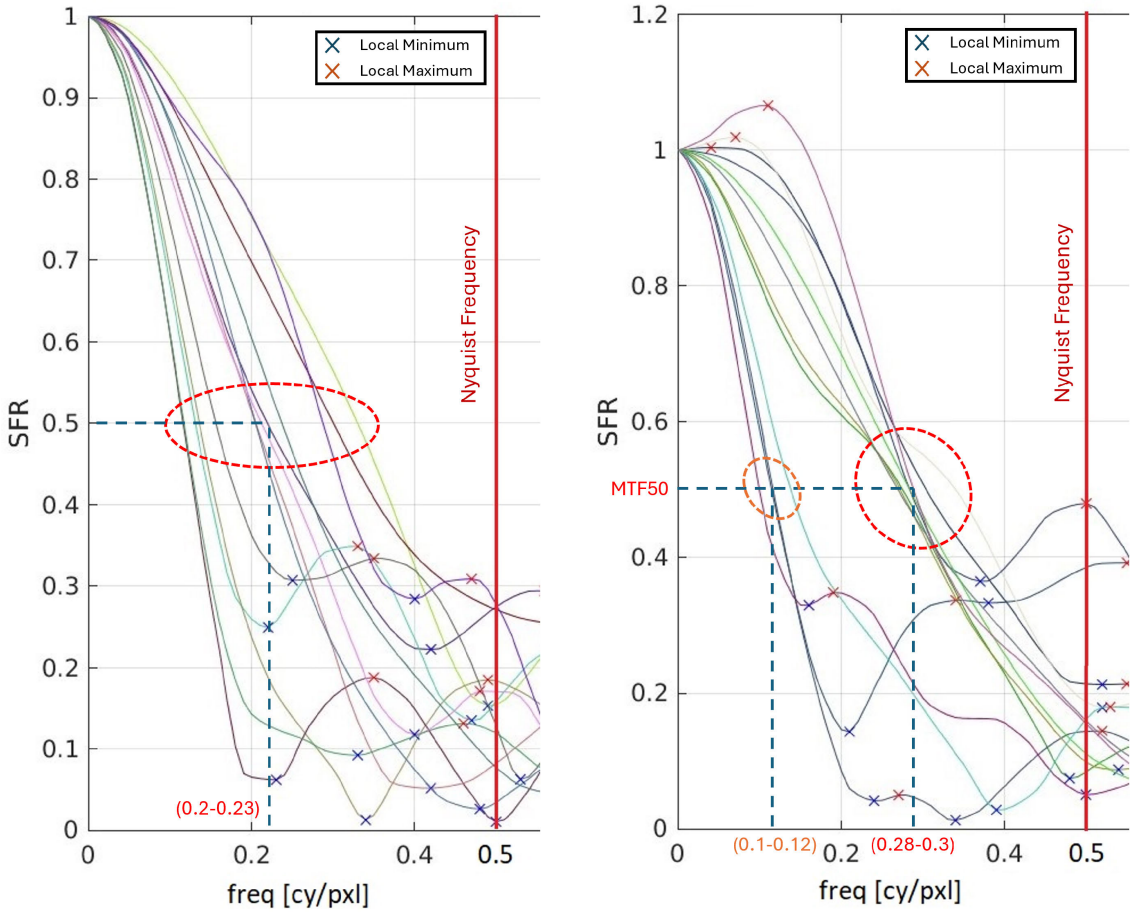

(a) **Unrectified Horizontal** (b) **Rectified Horizontal**

FIGURE 8. (a) Unrectified and (b) Rectified horizontal MTF measurements are compared in one instance of the second gray KITTI camera for horizontal edges using ISO12233:2023 [21]. Note: distortion is removed from the same scene in (b), where it clearly shows a positive boost in MTF50 values. A minority of MTF50 is clustered around 0.1-0.12cy/px. In contrast, the majority is tightly clustered around 0.28-0.3cy/px, which could show a trend of positive bias for rectified images (see Figures 6 and 7 for the qualitative results).

scenes [13]. Finally, we will present the CaRa Evaluation shown in Figure 10 of the entire KITTI images from Table 1 both with unrectified and rectified versions as a comparison.

1) KITTI ROI SELECTION

In Figures 6 and 7, a sample comparison is shown between slanted edge selection from a natural scene in KITTI where Figure 7 is rectified removing distortion from the original KITTI image. Each image has a valid and invalid ROI selection. An increasing number labels each candidate edge, i signifying that this is the i^{th} edge identified out of a potential n edges from the natural scene. Therefore, in the case of Figure 6 out of 64 potential edges, there are only 13 valid edges which represent approximately 20%. Likewise, in Figure 7, out of 60 potential edges, there are 12 valid slanted edges (representing the same ratio as before, but this depends on lighting conditions and pixel contrast, signifying the complexity of measuring from natural scenes). The measurements no longer represent the measurements of the actual camera lens. Any image manipulated in this manner can affect a valid slanted edge measurement, artificially inflating the results. As evidence of how distortion affects results, Figure 8 illustrates the difference for horizontal edge measurements. The shape of a typical slanted edge should resemble that of Muller et al. [42] experiments where MTF50 was approximately between the (0.07-0.2) range for both superposition and the isoplanar patches algorithm for PSF model approximations with square blocks of $320^2 pixels^2 (\mathrm{ISO}_{320})$ [42]. Natural Scenes measurements offer a more representative camera performance analysis over conventional test charts where the step edge of natural scenes does not result in an artificial e-SFR boost associated with test charts and non-linear processing where the inclusion of the surrounding scene reduces sharpening effects of e-SFRs [12]. Comparing MTFs

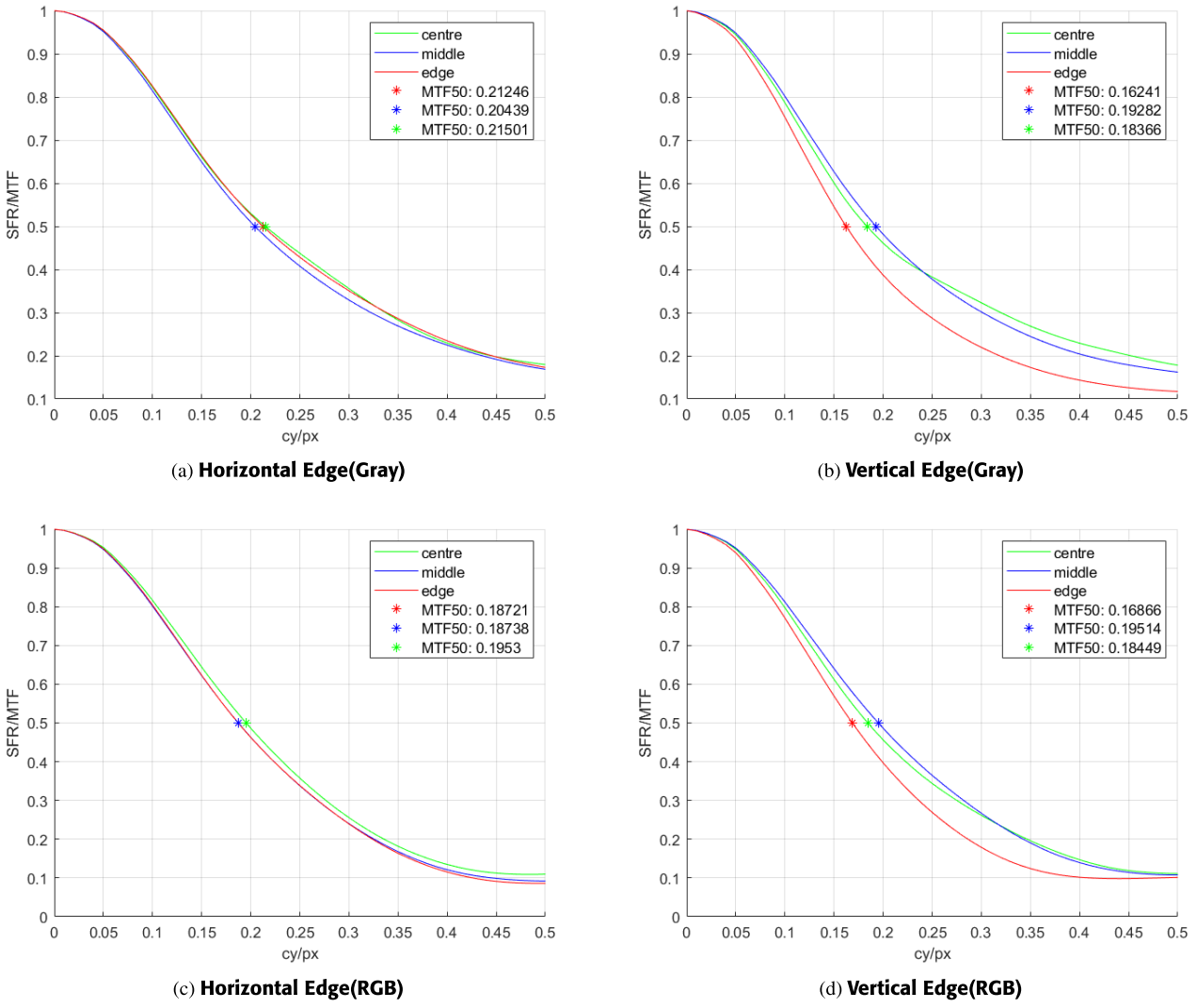

(a) **Horizontal Edge(Gray)** (b) **Vertical Edge(Gray)**

(c) **Horizontal Edge(RGB)** (d) **Vertical Edge(RGB)**

FIGURE 9. **MTF plots for KITTI CaRa of one grayscale (first row) and one colored (second row) using ISO12233:2023 [15] for horizontal and vertical edges in unrectified KITTI cameras with NS-SFR parameters (ST=0.02, esfW = 5).**

for both Figures 8a and 8b, the rectified cases overall give tightly clustered measurements. For unrectified KITTI, the MTF50 measurements are uniformly spread out showing a fair representation of results (see Figure 6 corresponding to 8a) whereas, the majority of slanted edge measurements for MTF50 would be tightly clustered around 0.1 and 0.3 cy/px (see Figure 7 corresponding to 7).

Also, the rectified scene has less pixel information at the periphery. In Figure 7, the car's wheel is now less visible in the foreground than in Figure 6. Eising et al. [2] illustrates the complexity of warping techniques for images with strong radial distortion and highlights the need to develop algorithms that natively address distortion rather than rectifying and manipulating the image data.

2) KITTI CaRa EVALUATION

In Figure 9, four MTF50 plots are shown where only the unrectified cameras are considered for this analysis due to the reasons outlined in the previous part of this section. We are only interested in the original unrectified images of KITTI, which contains the actual camera lens used for data collection. In this set of experiments, the 2nd and 4th cameras of KITTI are used, where one captures images in grayscale and the second in color. The 1st and 3rd cameras of KITTI have very similar results to that seen in Figure 9; hence, only showing results from two cameras would be sufficient in terms of assessment of outcomes. As shown in Figure 9, horizontal and vertical edges are captured from the same scenes where the image is divided up spatially into three CaRas (please see KITTI CaRa regions in Figure 10). The three radial segments can be classified as either center (green), middle (blue), or edge (red). Evidently, in Figure 9a and 9d, the shape of the MTF function largely resembles that of the MTF from Muller et al. [42] where MTF50 values are between 0.16-0.24 cy/px. This demonstrates the reproducibility of

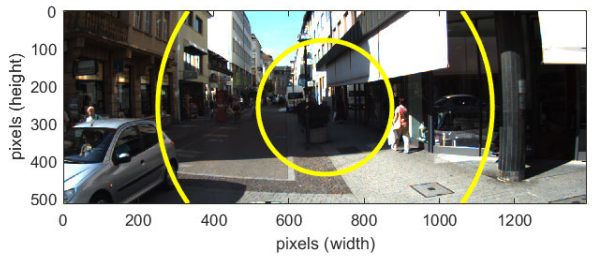

FIGURE 10. KITTI CaRa on 4th camera RGB).

results from Zwanenberg et al. [11] using the default NS-SFR parameters for step edge noise (ST=0.02) and Edge Spread Function Width (esfW = 5 pixels). Comparing the horizontal edges in the three segments in Figure 9a and 9c, MTF50 is higher for grayscale images by approximately 10.09% for the central segment (green), 9.08% for the middle segment (blue) and 13.49% for the edge (red) segment. However, for vertical edges in Figure 9b and 9d, the results are roughly the same where differences are less than or equal to 3.8% in each segment. Also, comparing horizontal edges in Figure 9a and 9c to vertical edges in Figure 9b and 9d, the majority of MTF50 results are higher for horizontal edges by a minimum of 5.86% than vertical edges (except for the middle segment for the colored camera where a lower MTF50 was recorded by 4.14%) indicating that for the KITTI images there tends to be a larger selection of horizontal edges over vertical edges as natural scenes tend to have more horizontal edges than vertical edges especially where in automotive driving the road has a majority of horizontal features (illustrating the scene-dependent properties of the NS-SFR).

B. KITTI-360

In this section, we will present the analysis of KITTI-360. KITTI-360 consists of two fisheye cameras with 180° FOV, each situated on the roof of the ego-vehicle aimed at both left and right perspectives as in Table 1. The spatial distribution of ROI selection of the left camera is considered in natural scenes in Figure 11. Finally, we will present both radial distance and heatmap analysis of KITTI-360 where a typical pattern is observed from the data.

1) KITTI-360 CaRa EVALUATION

In Figure 11, the spatial distributions of both horizontal and vertical edges are displayed with their respective mean MTF (see Figure 11c and 11d). Similar to the KITTI measurements, three radial distance segments classify the location of slanted edges in natural scenes where Figure 11c and 11d represent their equivalent mean MTFs for each segment. It was found that approximately the same image quality can be found in KITTI-360 as KITTI, indicating that despite the radial distortion that is introduced in KITTI-360, NS-SFR can extract edges successfully from the images regardless of location. Also, in KITTI, there are fewer vertical edges found in the natural scenes than there are horizontal edges when comparing Figure 12a to 12c. This does not affect slanted edge measurements significantly where the differences between MTF50 measurements between Figure 11c and 11d for each segment is within 1.491% where horizontal edges are slightly higher in quality than vertical edges. One distinct effect is evident in the KITTI-360 images is the spread of MTF graphs where the central segment (green) has the sharpest slanted edges with MTF50 of around (0.19305-0.1957) cy/px, followed by the middle segment (blue) of between (0.18031-0.18309) cy/px and finally the edge segment (red) of between (0.15344-0.16835) cy/px. This would be an expected result as distortion is less evident at the center than at the periphery.

2) KITTI-360 O'SHea EVALUATION

As a means of further insight into MTF50 measurements, a heatmap analysis was performed on the spatial domain of KITTI-360 using 8 × 5 heatmap regions where the corner four regions i.e., (1,1), (8,1), (1,5) and (8,8) are ignored (see Figures 11a and 11b where the corner regions of the grid are outside the natural scene). Heatmaps are powerful tools where patterns can be observed in each image region. In this case, we calculate the mean MTF plot for each region where slanted edge locations fall into the heatmap region. The heatmap regions are then classified into three categories depending on their location in the spatial domain, similar to the CaRa Evaluation in the previous section. The heatmap regions are evaluated according to the segments of CaRa. The centroids of each heatmap region are isolated, and depending on where they fall in the radial segments, they are categorized as central, middle, or edge. As shown in Figure 11b, two regions are classified as central (green), 12 regions are classified in the middle (blue), and finally, 22 regions are at the edge (red). O'SHea heatmaps can be referred back to the locations from 11b, which is directly comparable to 12. The MTF plots in 12a and 12c have corresponding heatmaps in Figure 12b and 12d. As can be seen from Figure 12b, edge segments have the widest range of slanted edges (i.e., 0.149-0.199 cy/px), middle segments have the second widest (i.e., 0.176-0.210 cy/px) and finally, the central segments have the narrowest range (i.e., 0.202-0.204 cy/px). The highest MTF50 score for the middle segment was recorded at 0.210 cy/px, illustrating that a few outliers may affect results. Due to the wider range of scores in the middle segment, this outlier is not apparent in the mean score for CaRa results. Similarly, in Figure 12d, edge segments have the widest range of slanted edges (i.e., 0.150-0.197 cy/px), middle segments have the second widest (i.e., 0.170-0.210 cy/px) and finally, the central segments have the narrowest range (i.e., 0.203-0.204 cy/px). This illustrates the usefulness of both methods for spatial domain analysis, where the heatmap technique provides greater insight into the overall results on a region-by-region basis. See additional results for the right camera in Figure 28 appendices.

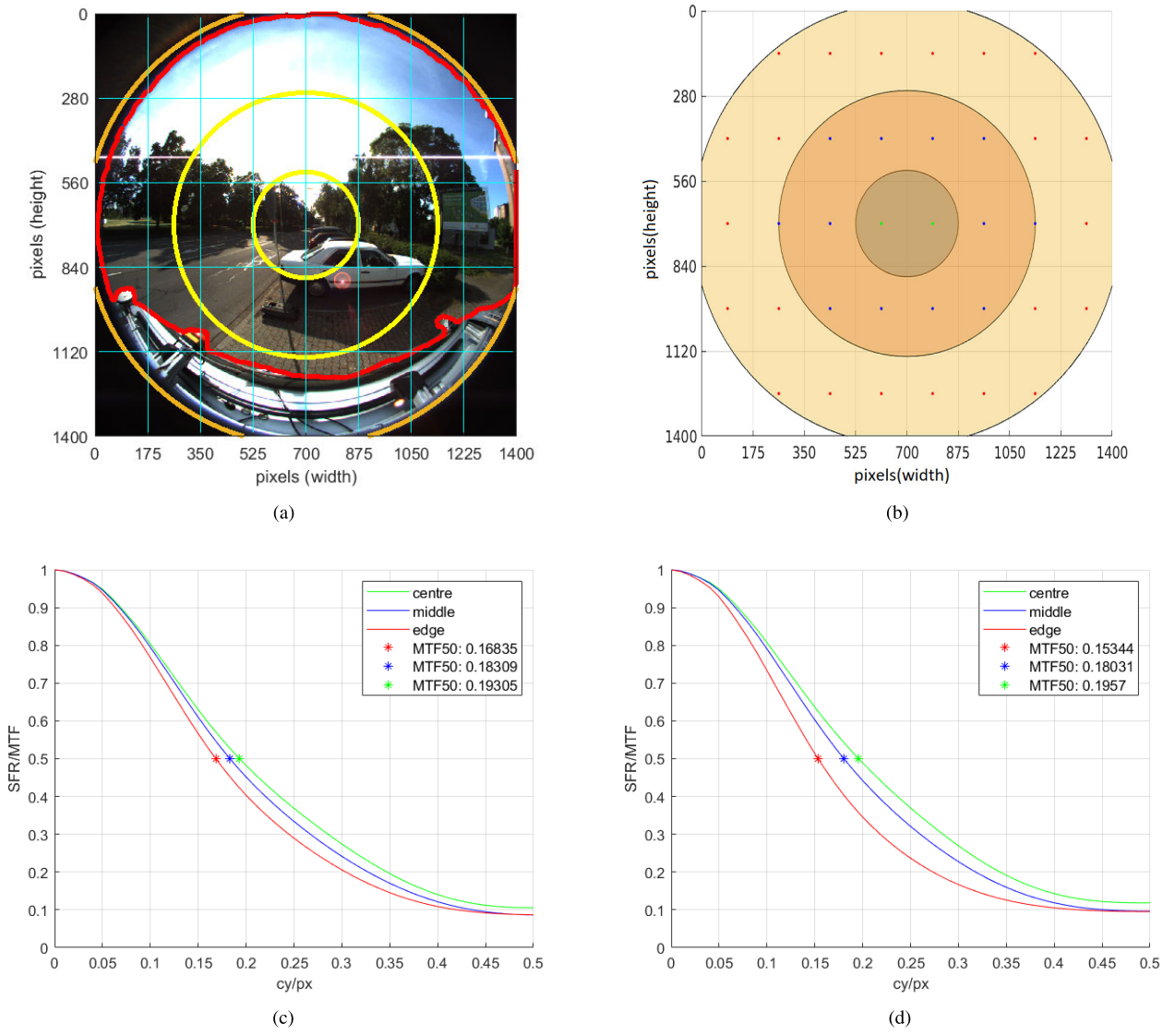

FIGURE 11. MTF plots of KITTI-360 CaRa using ISO12233:2023 [21] on the left camera with NS-SFR parameters of (ST=0.02, esfW=5) with (a)CaRa: Inner (yellow) and outer (orange), RMLA(red) and 8 × 5 O'SHea(cyan grid), (b)O'SHea Heatmap centroid locations with respect to CaRa, (c) Horizontal Edge MTF plot and (d) Vertical Edge MTF plot.

C. LMS

In this section, we will present the analysis of the LMS dataset, which has a circular fisheye aperture similar to KITTI-360. LMS consists of a single rear-facing fisheye camera with 185° FOV situated at the rear bumper of the vehicle. The main purpose of testing on the second circular fisheye camera is to identify any patterns in results and whether the KITTI-360 results can be replicated by varying the scene. Compared to KITTI-360, we get a different ROI selection pattern.

1) LMS CaRa EVALUATION

In Figure 14, the spatial distributions of both horizontal and vertical edges are displayed with their respective mean MTF for each radial segment (see Figure 14a and 14c). Similar to KITTI-360, the pattern of ROI selection more or less follows the degree of distortion in the camera (notice that the spatial distributions of both horizontal and vertical slanted edge locations follow a pattern of upsidedown parabolic shapes which straighten out as they reach the center and are inverted from center to the bottom of the spatial domain). However, in contrast to KITTI and KITTI-360, there were much more valid ROIs found above the ground in the spatial domain (see Figures 14a and 14c where the density of points is much less above the road (see Figure 14a where from approximately >651.6 pixels on the y-axis, there is an outline of the road visible which visually can be seen in Figure 13a at approximately the same pixel range). Figure 13a also clearly shows a parked car on the left-hand side of the road. This

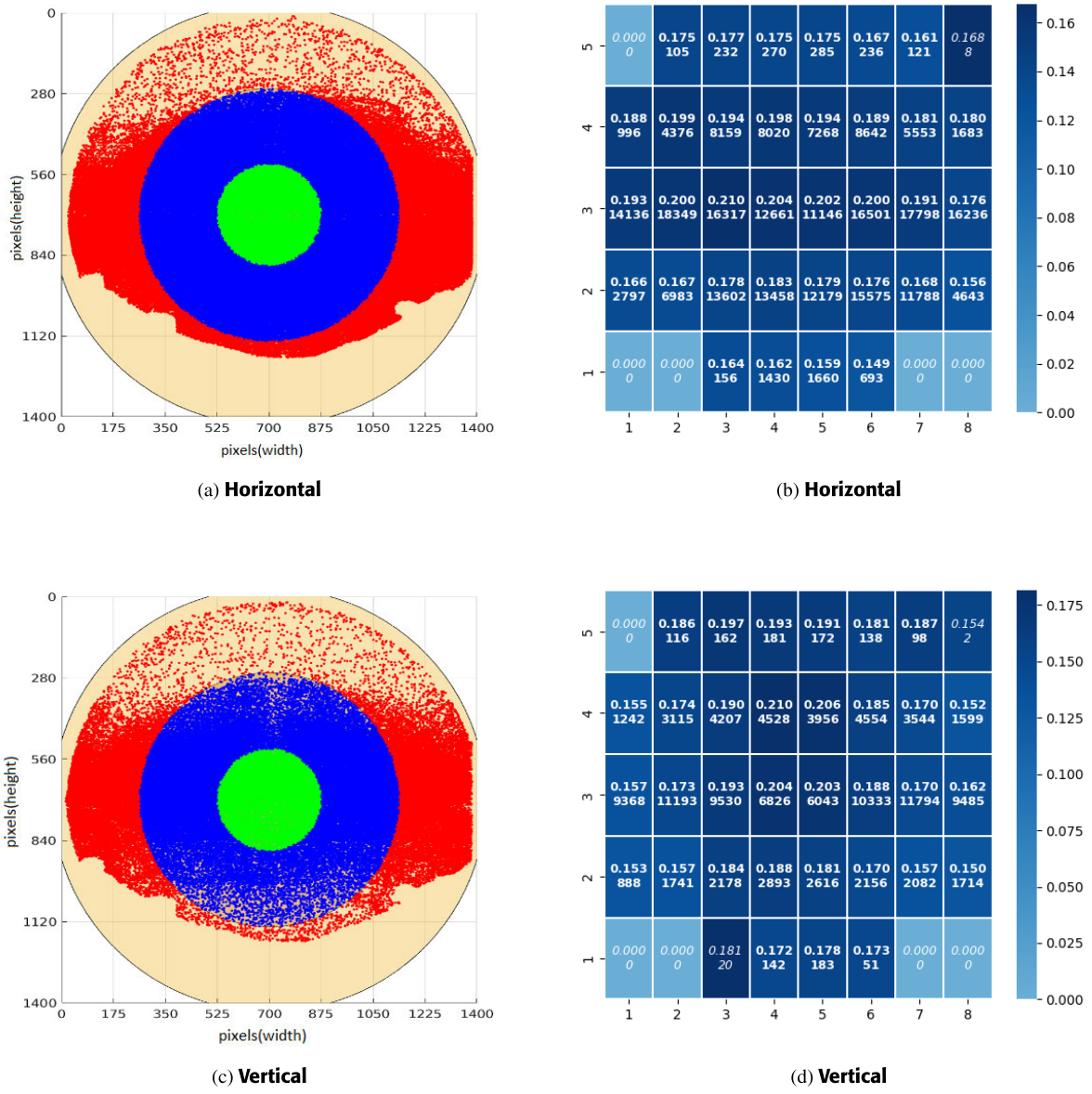

(a) **Horizontal** (b) **Horizontal**

(c) **Vertical** (d) **Vertical**

FIGURE 12. KITTI-360 Spatial Distribution and O'SHea MTF50 Analysis for ISO12233:2023 [21] on the left camera with NS-SFR parameters of (ST=0.02, esfW=5). Note: Colors represent the spatial domain location according to CaRa (see Figure 11), i.e., center (green), middle(blue), and edge(red). Each region displays the mean MTF50, and the number of data points found where <20 samples are shown in italics.

means that due to the camera position or the position of the ego-vehicle, the camera will tend to capture more slanted edges of the parked cars situated on the left side than the right side due to proximity and better visibility of the edges on those vehicles. This gives rise to the phenomenon observed in Figure 14a where a cluster of points is located in the regions $(x, y) = (143.75 \longleftrightarrow 431.25, 651.6 \longleftrightarrow 868.8)$ pixels which are situated at the left-hand side of the road as in Figure 13a. Also, the quality of MTF50 results more or less resembles both KITTI and KITTI-360 results (see Figures 13c and 13d). The main difference is the spread of MTF graphs compared to KITTI-360. When comparing Figure 13c to 11c, LMS has an opposite spread of MTFs that are higher quality edges found at the periphery of the camera than at the center, which is unexpected behavior. However, for vertical edges, both Figures 11d and 13d are approximately the same with LMS containing slightly higher mean MTF50 with a minimum of 8.5% improvement for the central segment. The contrasting behavior in both horizontal and vertical instances might suggest that CaRa Evaluation alone is not sufficient to understand natural scenes. Using CaRa Evaluation alone does not give clear insight as to

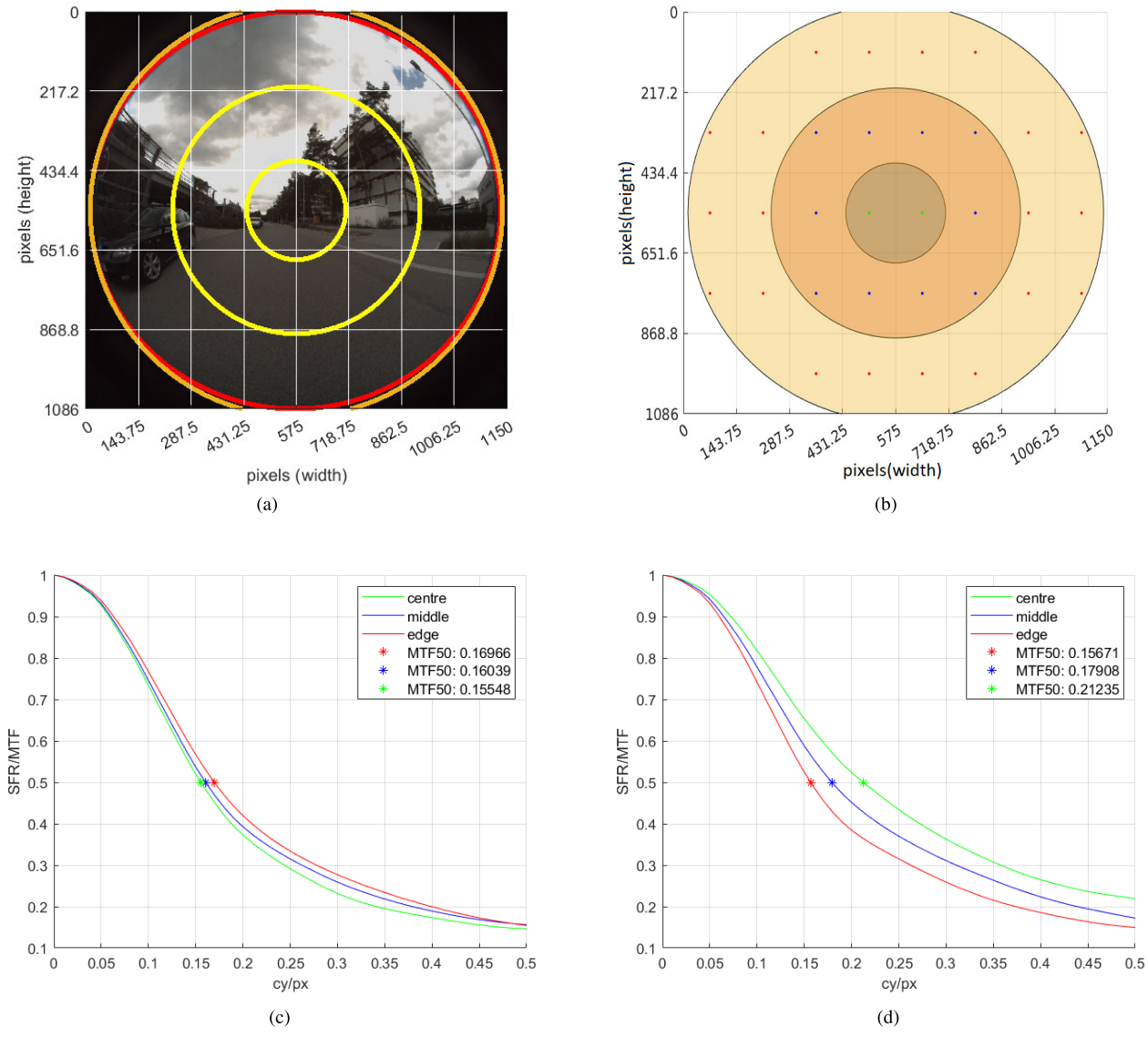

FIGURE 13. MTF plots of LMS using ISO12233:2023 [21] with NS-SFR parameters of (ST=0.02, esfW=5) with (a) CaRa: Inner (yellow) and outer (orange), RMLA (red) and 8 × 5 O'SHea (cyan grid), (b) O'SHea Heatmap centroid locations concerning CaRa, (c) Horizontal Edge MTF plot and (d) Vertical Edge MTF plot.

why the periphery cases would be higher than central cases. Therefore, the spatial domain should be separated and analyzed by region, as would be possible in heatmaps. Therefore, it is much more useful to look at heatmap results in this case than CaRa results.

2) LMS O'SHea EVALUATION

The spatial distribution of LMS is shown in Figure 13b. In both Figures 14b and 14d, further analysis of LMS shows that slanted edge selection is completely different once the camera is positioned closer to the ground, unlike KITTI-360 where cameras were positioned on top of the vehicle. It is also worth noting that the KITTI dataset has minimal distortion. Therefore, the spread in results was not as obvious as is for LMS, which is a fisheye camera. The heatmaps from Figure 14b and 14d show that better quality MTF50 measurements can be found on the ground from a cell range of between $(x, y) = (1 \longleftrightarrow 8, 1 \longleftrightarrow 2)$ inclusive, except for the corner cells of $(x, y) = (1, 1)$ and $(x, y) = (8, 1)$ where 0 or 1 data points are found. Notably, cells $(x, y) = (5, 2)$ and $(x, y) = (6, 2)$ have the highest MTF50 scores for both horizontal and vertical edges. To illustrate how large this contrast is, we can see the following observations. For horizontal edges in Figure 14b, heatmap regions below the 2^{nd} row of the heatmap show MTF50 values which increase from regions above the 2^{nd} from between (0.137-0.234) cy/px to (0.247-0.366) cy/px. This is an improvement of about

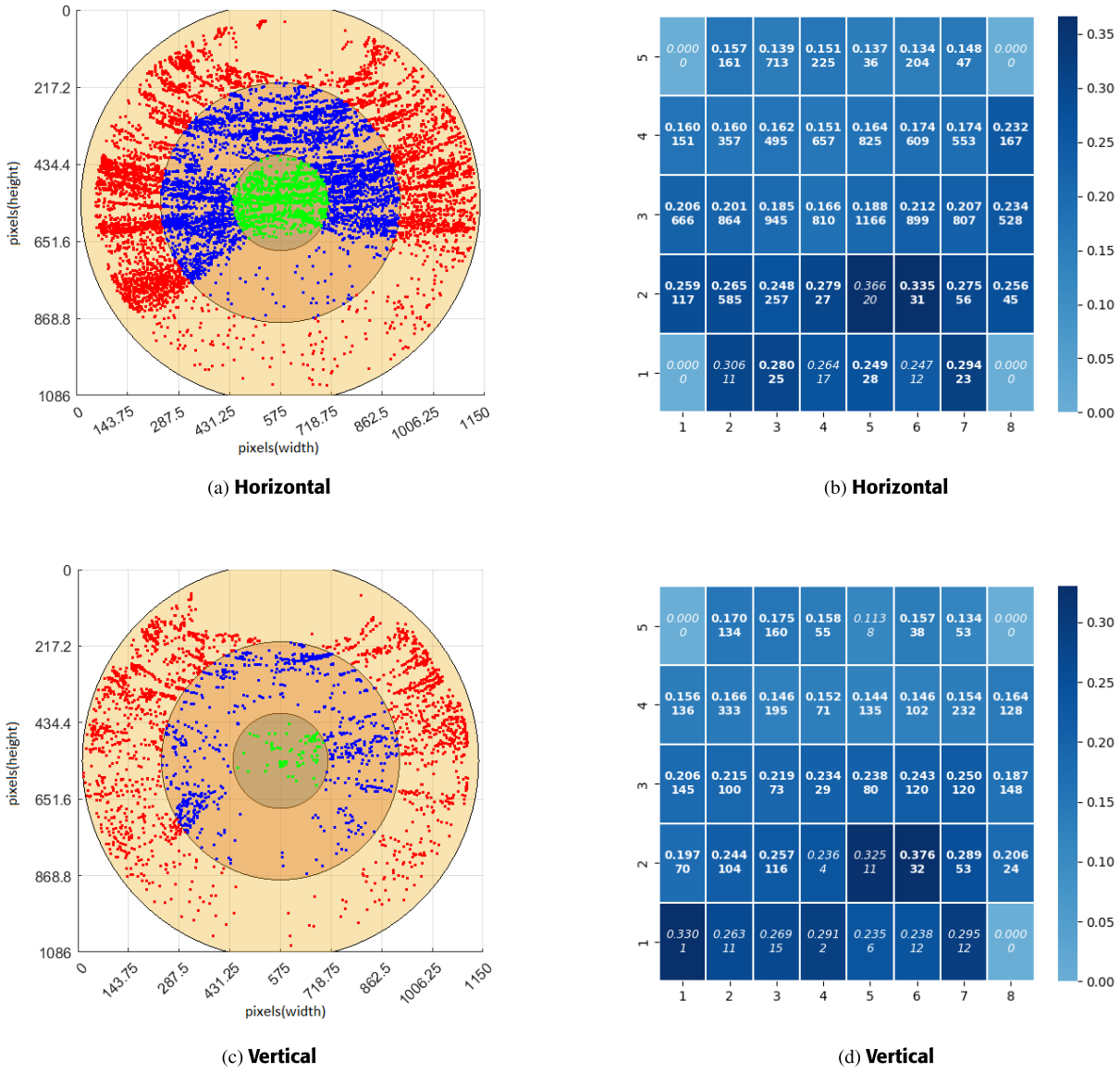

(a) **Horizontal** (b) **Horizontal**

(c) **Vertical** (d) **Vertical**

FIGURE 14. **LMS Spatial Distribution and O'SHea MTF50 Analysis using ISO12233:2023 [21]. Rear View camera with NS-SFR parameters of (ST=0.02, esfW=5). Each region displays the mean MTF50, and the number of data points found where <20 samples are shown in italics.**

44.53% in the minima and 36.07% in the maxima cases. Similarly, for vertical edges in Figure 14d, heatmap regions below the 3rd row of the heatmap show MTF50 values which increase from regions above the 3rd from between (0.113-0.175) cy/px to (0.187-0.376) cy/px. This is an improvement of 39.57% in the minima and 53.46% in the maxima case.

The heatmap results clearly show a distinct impact on mean MTF50 CaRa results from Figure 13a, where scene dependence could be a key contributing factor. If higher MTF50 slanted edges can be found on the ground than in the sky, the two contrasting trends will unpredictably influence any radial distance measurement. Perhaps this shows that heatmap analysis is more effective in automotive scenes than CaRa Evaluation, especially if the fisheye camera is positioned just above the road, as is in most automotive scenes.

D. WOODSCAPE

In this section, we will present the analysis of Woodscape where, unlike KITTI-360 and LMS, this dataset is calibrated using the 4th order polynomial projection model [20]. Woodscape consists of four perspectives, mainly FV, MVL, MVR, and RV, as shown in Table 1 where, out of the available perspectives, the dataset was split up into roughly the same number of samples. Woodscape has a slightly wider FOV at 190°, which allows for capturing more of the natural scene, implying a 360° surround-view system. Using the fine-tuned parameters from KITTI-360, We apply the adapted NS-SFR

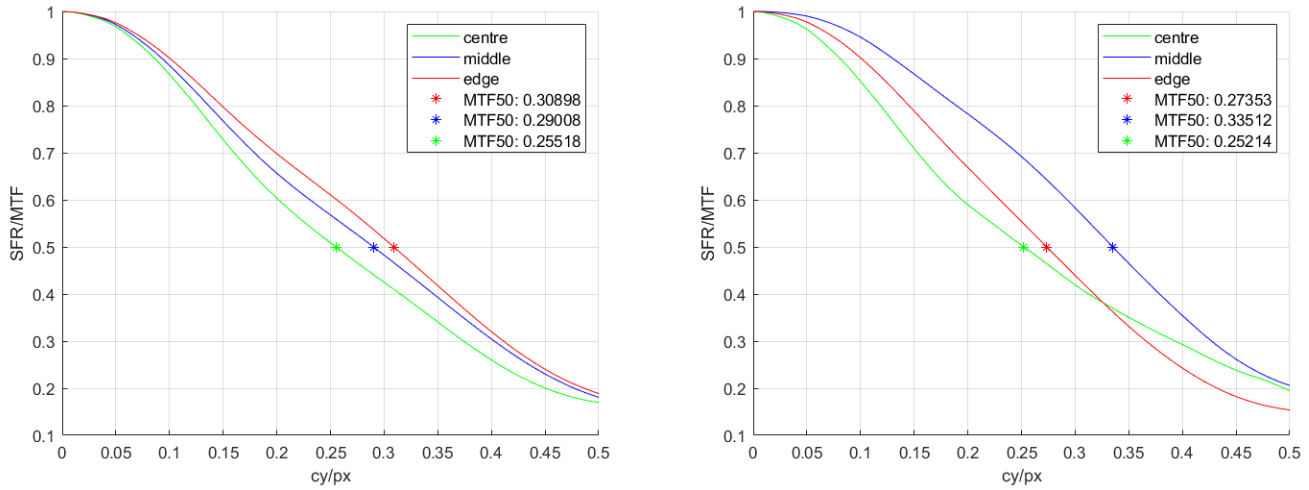

(a) **Horizontal** (b) **Vertical**

FIGURE 15. MTF plots of Woodscape CaRa Evaluation using ISO12233:2023 [15] of Front View (ST=0.02, esfW=5). First row: horizontal edges, Second row: vertical edges.

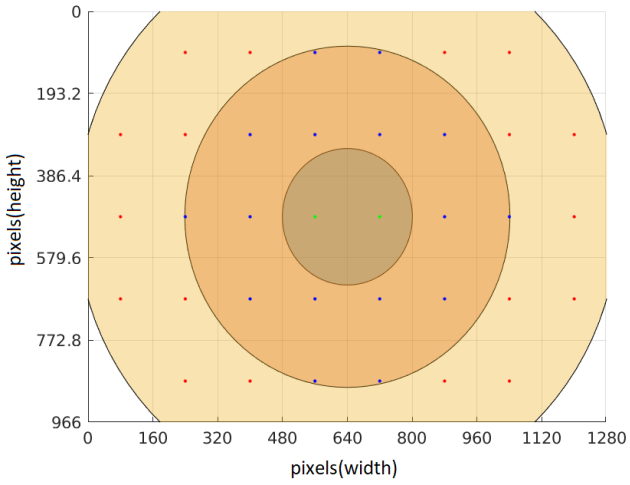

FIGURE 16. O'SHea: Heatmap Spatial Locations for Woodscape.

to all four perspectives, observing how this differs from the previous two fisheye datasets.

1) WOODSCAPE CaRa EVALUATION

In Figure 17, the spatial distributions of both horizontal and vertical edges are displayed with their respective mean MTF for each radial segment (see Figures 15a and 15b). The FV of Woodscape for horizontal and vertical edges are compared (i.e., the first sample of 1514 images from Table 1). In contrast to LMS, the pattern of ROI selection for horizontal edges follows the horizon where the ground meets the sky and the foot of buildings (see Figure 17a). Also, most vertical edges are found on both sides of the spatial domain, suggesting that buildings on both sides of the road contain better edges than the center (see Figure 17c), which is expected. Interestingly, when comparing Figure 15a to 11c there is a significant improvement in MTF50 of more than 32.18% in all segments.

Similarly, the MTF50 for vertical edges in all segments improved by more than 28.84% when comparing Figure 15b to 11d. There may be several reasons behind this improvement. A major reason could be that the positions of both KITTI-360 and Woodscape cameras are completely different, where KITTI-360 is positioned on top of the vehicle, and Woodscape is positioned close to the ground. It has already been demonstrated via LMS (see previous section V-C) that scene dependence affects measurements, especially if the camera is close to the ground (see Figure 14). This implies that Woodscape measurements are better mainly because there is a better selection of slanted edges on the ground than above the vehicle. This indicates that NS-SFR should be limited to specific camera positions, mainly complete ground or sky, to avoid conflicting results. A selection strategy could also be determined where a cluster of results could be categorized based on the background information of the natural scene. For example, if the objects on the ground were more of a priority, then image quality must be as high as possible for objects to be recognized in computer vision algorithms. Therefore, if the MTF values on the road and the buildings are reasonably high between (0.25-0.3) cy/px (as is the case for horizontal edges in Figure 15a), then the lens is considered to have sufficient image quality for this purpose. However, a more detailed analysis is needed to differentiate the contents or objects of the road for greater insight. For example, detecting edges on cars may be different from the road in shadow measurements.

2) WOODSCAPE O'SHea EVALUATION

The spatial distribution of the front view of Woodscape is shown in Figure 16. The heatmaps for Woodscape for both

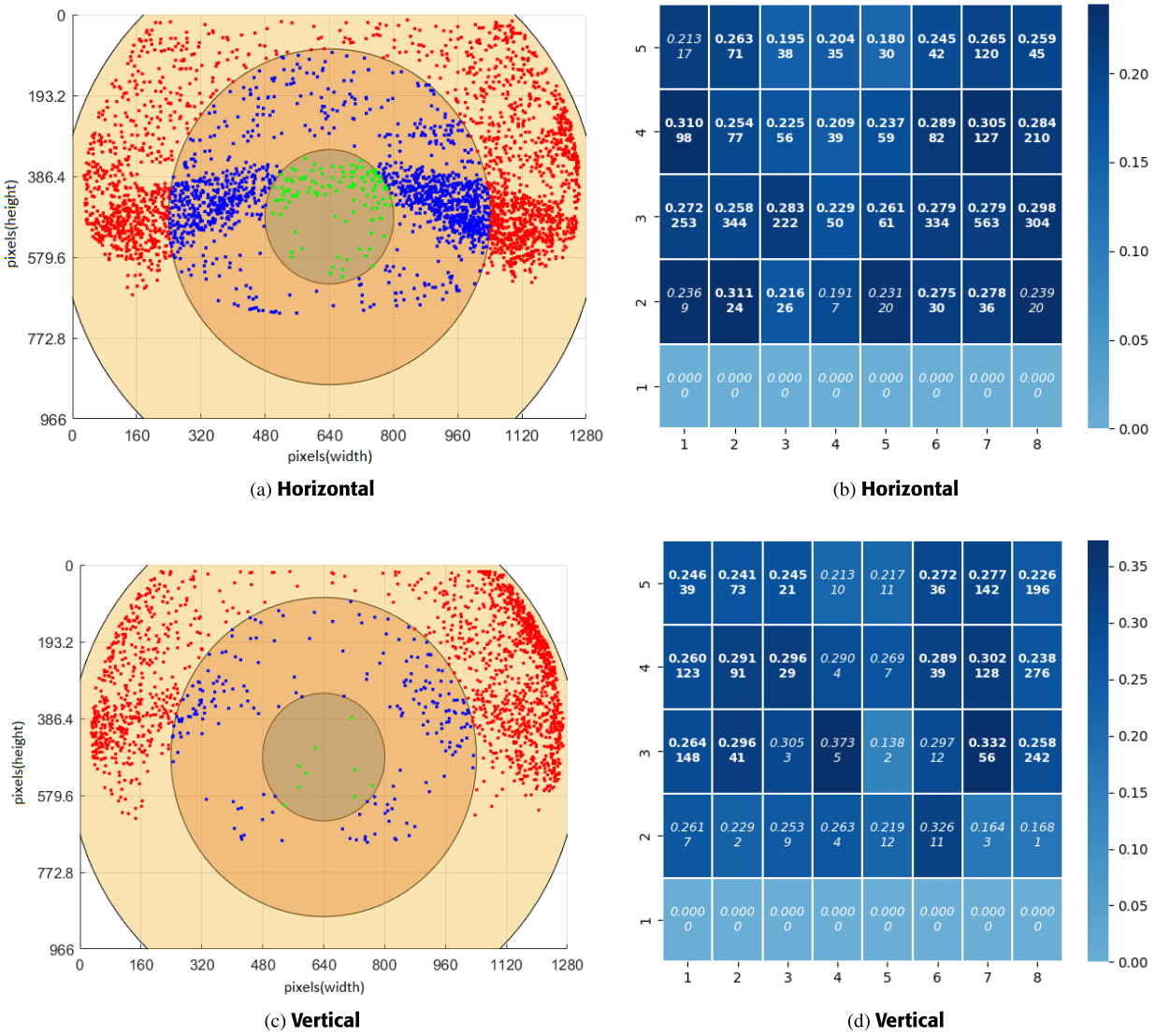

(a) **Horizontal** (b) **Horizontal**

(c) **Vertical** (d) **Vertical**

FIGURE 17. **Woodscape Spatial Distribution and O'SHea MTF50 Analysis using ISO12233:2023 [21] of the Front View with NS-SFR parameters of (ST=0.02, esfW=5). Each region displays the mean MTF50, and the number of data points found where <20 samples are shown in italics.**

horizontal and vertical edges show no distinct pattern where both edge and middle regions have roughly overlapping MTF measurements (see Figures 17b and 17d). There is no distinct pattern like that of KITTI-360 (see Figures 12a and 12c). However, the heatmaps offer a different perspective; for horizontal edges, the four highest MTF50 heatmap region values (i.e., 0.311, 0.310, 0.305, and 0.298) can be near or on the periphery of both the left and right of the spatial domain. In contrast, for vertical edges, the six highest values (i.e., 0.373, 0.332, 0.326, 0.305, 0.302, and 0.297) can all be found towards the center or middle of the spatial domain (more specifically along the horizon of the road). For vertical edges, the center segment has the highest mean MTF50 value of 0.373 cy/px, which is at least 11.7% higher than either edge or central segments, as shown in Figure 15b. These results can be considered counter-intuitive, where two completely different sets of behaviors are found for image quality. A possible explanation for this phenomenon is the effect of distortion on the spatial domain, where apparently, distortion has sharper horizontal edges in natural scenes towards the periphery. In contrast, sharper vertical edges can be found at the center or middle spatial domain. A limitation to the observation of the vertical edges is that there are less than 20 data points isolated in the central regions of the spatial domain. In contrast, the periphery regions have 40+ data points, suggesting higher confidence in the periphery results than the center (likely due to the higher probability of finding vertical edges on the buildings towards both sides of the road). Results are inconclusive because the dataset is small, and more fisheye datasets are needed to verify this trend for natural scenes.

E. SYNWOODSCAPE

In this section, we will present the analysis of SynWoodscape (a synthetic version of Woodscape created in CARLA [24]), which is calibrated using the 4^{th} order polynomial projection model as in Woodscape and the cube map projection model [23]. Similar to Woodscape, SynWoodscape consists of four perspectives, mainly FV, MVL, MVR, and RV, as shown in Table 1 where out of the available perspectives, the dataset was split up into the same number of samples (i.e., 500 images for each perspective). Like Woodscape, SynWoodscape has a wide FOV of 190°. We use the same parameter from the Woodscape experiments as a means to investigate the difference between both real life and simulation. In this section, all scenes can be considered synthetic scenes as a way of differentiating from real life with natural scenes.

1) SYNWOODSCAPE CaRa EVALUATION

In Figure 19, the spatial distributions of both horizontal and vertical edges are displayed with their respective mean MTF for each radial segment (see Figure 18c and 18d). The FV of SynWoodscape for horizontal and vertical edges are compared (i.e., the first sample of 500 images from Table 1). There is a drop in MTF50 values for both horizontal and vertical edges when comparing Figure 18c to 15a where there is a 29.03% to 54.36% drop across all three segments. Similarly, when comparing Figure 18d to 15b, there is a 24.68% to 50.74% drop across all three segments. This suggests that simulation while generating much more ideal slanted edges, measurements do not reflect reality and, in the case of SynWoodscape, can produce results incomparable to the measurements in real life. This is an expected result mainly because SynWoodscape only applies distortion to the simulated images and does not carry over the actual lens properties into the simulation, highlighting the limitations of current simulation models.

2) SYNWOODSCAPE O'SHea EVALUATION

The spatial distribution of the front view SynWoodscape is shown in Figure 18b. In Figure 19, the 8×5 regions of the spatial domain are displayed alongside the values in heatmap regions for both horizontal and vertical edges. Comparing both Figures 19a and 19c, there are some similarities to the spatial distribution of results for the three radial segments (see Woodscape distributions in Figures 17a and 17c). Both horizontal spatial distributions show most slanted edges clustered along the road's horizon. Vertical distributions both show left and right peripheries with more slanted edges. However, the quality of edges is approximately the same (if not slightly better than) the KITTI measurements from Section V-A where values were between (0.16-0.22) cy/px. This shows that results are incomparable to Woodscape, and there is still a long way to go when modeling lenses in simulation. Furthermore, the heatmaps in Figures 19b and 19d suggest no conclusive patterns emerging from the spatial domain. The only observation that can be made is that there are mostly higher MTF50 values found above the ground, which contradicts behavior from Section V-D. As an example, one might argue that stronger MTF50 values for vertical edges can be found above the ground along row 5, where the three highest values exist in coordinates (7,5), (2,5), and (6,5), respectively (see Figure 19d). Further investigation is required to prove this fact and once again shows the contrastive effects of distortion on both simulation and real life. For additional results, please see Appendices.

F. DISCUSSION

In this section, we will discuss results from all five datasets. The results shown in this work give confidence, whereas results recorded in heatmap regions give > 20 data samples, suggesting a robust set of results in most cases. There can be a few observations from the results shown in this section:

1) Rectified KITTI measurements have a higher overall set of MTF50 values than the original KITTI (see Figure 8 and Table 2 in Appendices). This can be due to the nature of the rectification, which could artificially boost results, and it is clear that the results no longer represent the actual lens in the scenes.
2) In comparing both grayscale and RGB cameras, results are similar, settling around the 0.15-0.2cy/px mark. A few peculiar patterns are emerging where horizontal edges are slightly higher for grayscale, whereas for vertical edges, RGB has slightly higher values (see Figure 9).
3) KITTI-360 results contain the most data out of all possible experiments and clearly show a consistent pattern in both cases where the center of the lens has higher MTF50 results than the periphery (see Figure 12).
4) In contrast to KITTI-360, a clear scene-dependent scenario emerges for LMS results where from the heatmaps for both horizontal and vertical edges, there are slightly higher MTF50 results recorded below the horizon. Additionally, in this area, fewer edges were recorded, which could indicate that the lower results above the horizon are more reliable than those on the ground. Interestingly, the LMS CaRa distribution follows a geometric pattern in results where data points form parabolas or circle-like rings above the ground (see Figure 14).
5) Woodscape results show strong patterns where most of the horizontal edges can be found either along the horizon, the ground, or the buildings, which are unlike KITTI-360 or LMS. For vertical edges, most measurements can be found along the buildings in scenes, especially for front-view and rear-view cameras, and are noticeably scarce compared to horizontal measurements (see Figures 17 and Figures 21, 22 and 23 in Appendices).
6) SynWoodscape follows the same observations as Woodscape however, MTF50 results are lower in most

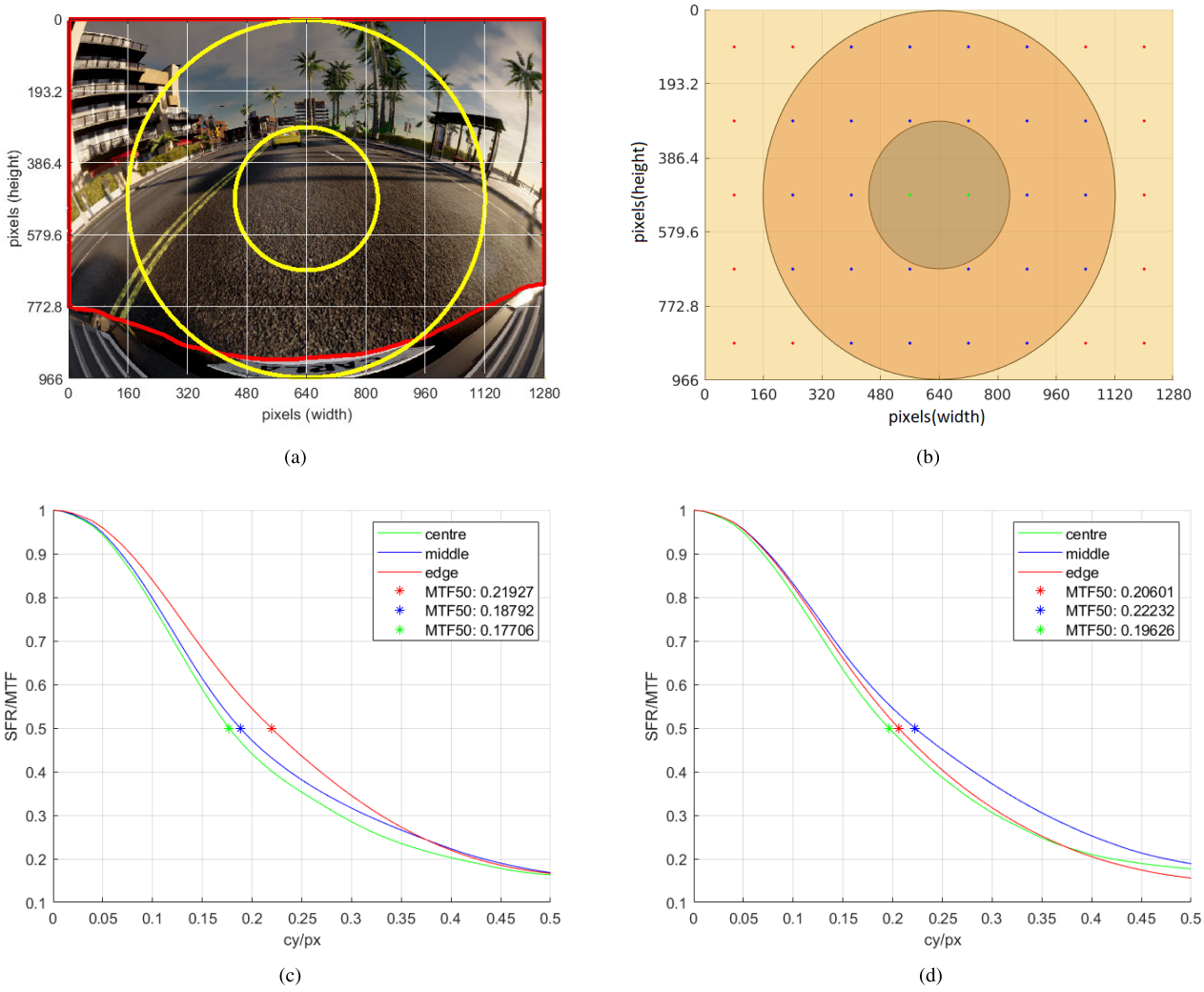

FIGURE 18. MTF plots of FV SynWoodscape CaRa using ISO12233:2023 [21] with NS-SFR parameters of (ST=0.02, esfW=5) with (a) CaRa: Inner (yellow) and outer (orange), RMLA(red) and 8 × 5 O'SHea (cyan grid), (b) O'SHea Heatmap centroid locations with respect to CaRa, (c) Horizontal Edge MTF plot and (d) Vertical Edge MTF plot.

cases than Woodscape, suggesting a clear gap between simulation and reality (please see Figures 19 and Figures 25, 26 and 27 in Appendices).

VI. LIMITATIONS AND FUTURE WORK

This study has shown it is possible to measure camera sharpness from public datasets using the Slanted edge method [21]. From this work, three observations can be made and should be explored in future work:

1) Camera sharpness is insufficient to evaluate cameras in all applicable scenarios quantitatively. As stated in recent work by Wolf et al. [4], if the camera is placed behind a windscreen, MTF50 measurements no longer represent those of the camera itself but that of a combination of both the camera and the windscreen. In future work, the BDD100k dataset [43] released publicly effectively recreates this same scenario where all images of the dataset are taken behind the vehicle's windscreen. This provides an additional set of experiments to investigate how the windscreen affects MTF50 measurements in a real-world automotive dataset. Based on the findings of Wolf et al. [4], a reasonable assumption to make would be that the MTF50 measurements from BDD100k [43] would be affected negatively for horizontal slanted edges and positively for vertical slanted edges due to two different focus offsets of the combined system. Observations from Wolf et al. [4] show that placing a windscreen in front of the camera cancels both offsets, leading to a sharpened camera system in practice.
2) The lack of publicly available automotive fisheye datasets, especially for automotive simulation, limited the selection of the experiments in this study. Generally, each camera perspective should have a large number of images available to obtain a strong measurement pattern. With more images, the measurements performed

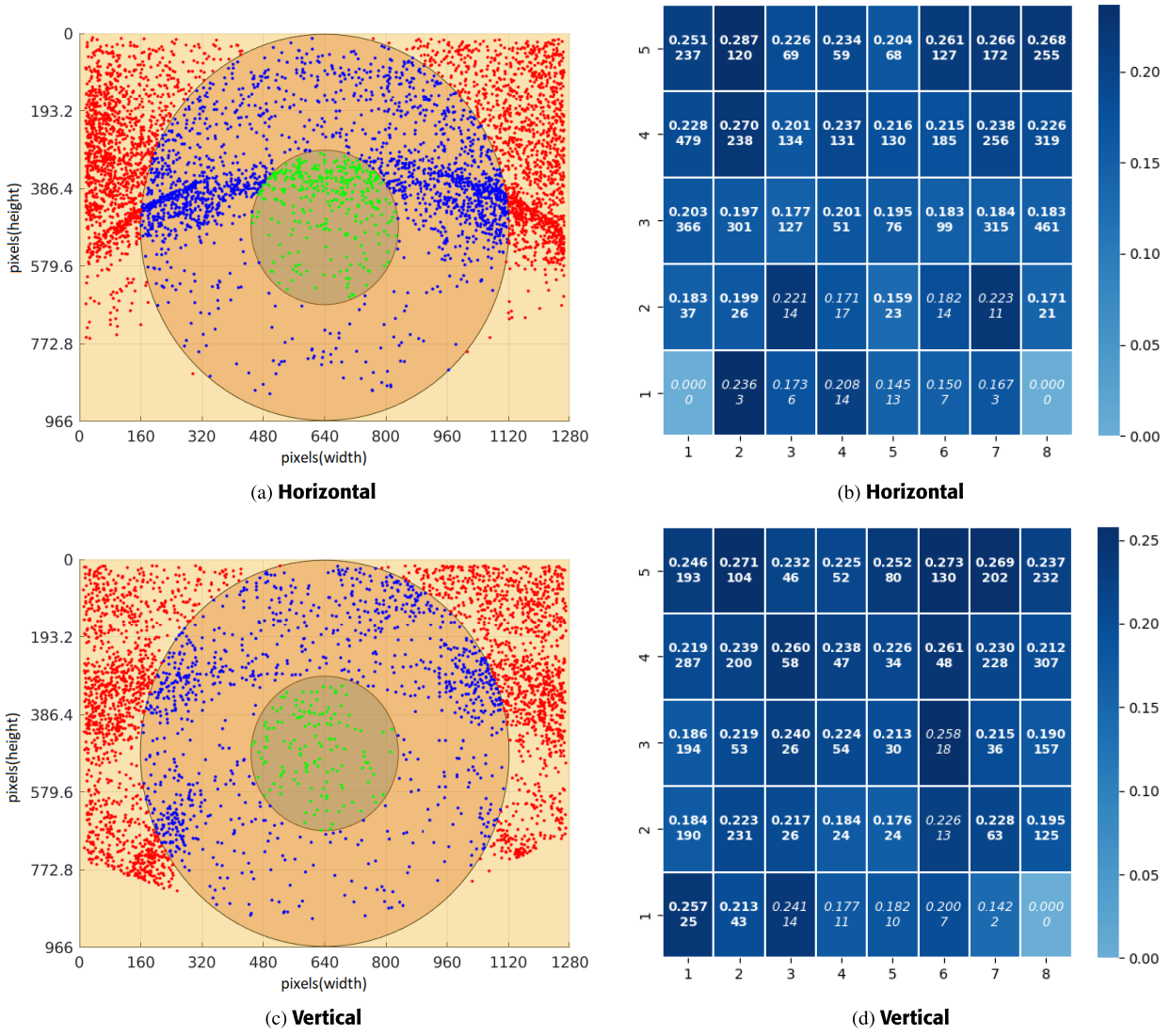

(a) **Horizontal** (b) **Horizontal**

(c) **Vertical** (d) **Vertical**

FIGURE 19. SynWoodscape Spatial Distribution and Heatmap Analysis using ISO12233:2023 [21] of the Front View camera with NS-SFR parameters of (ST=0.02, esfW=5). Each region displays the mean MTF50, and the number of data points found where <20 samples are shown in italics.

in the datasets would better estimate the camera's actual performance, suppressing outliers and any noise that may otherwise affect the measurements in small datasets.

3) Future work should introduce image quality metrics from the slanted edge and other relevant metrics for computer vision applications. Extending optical quality measurement strategies from natural scenes can bridge the gap between optical quality and computer vision performance. Recent works [25], [44] demonstrate that economic success depends on understanding the relationship between optical quality, defining camera production tolerance limits, and computer vision algorithm limits. For example, Noise Equivalent Quanta (NEQ) is an optical quality metric that stems from MTF and is a frequency-dependent Signal-to-Noise (power) ratio [45], [46]. Also, the newly proposed toolkit of image quality metrics by the research community [47], [48], [49] have not been sufficiently assessed for automotive driving linking Artificial Intelligence (AI) to optical systems performance.

VII. CONCLUSION

In this paper, we have performed optical quality measurements from both real-life and simulation scenes in five publicly available automotive datasets with varying degrees of FOV (i.e., 90°, 180°, 185°, and 190°, respectively) using ISO12233:2023 [21] version of the Slanted Edge Method. This was done by applying regional masks to camera perspectives (e.g., RMLA), selecting and categorizing the

spatial locations of valid regions for measurement using both CaRa and O'SHea techniques, and determining a set of constraints for MTF results (e.g., Slo-MTF and EiLíN). These contributions show that it is possible to measure and obtain a valid set of measurements to evaluate public automotive datasets using different camera systems, including fisheye. In the experiments performed, lenses with uniform spatial domains (i.e., little distortion) showed that MTF50 was constant between (0.18-0.25cy/px). With image rectification on the same scenes, MTF50 results artificially increased, no longer representing the camera lens. In contrast, for strong radial distortion, MTF50 varied extensively across the spatial domain between (0.12-0.4cy/px), where, in particular, Woodscape gave the highest average of MTF50 per region for natural scenes. Results show that it is possible to extract optical quality measurements from wide FOV cameras, which compare in quality to the camera used. Additionally, geometrical and scene-dependent patterns can be observed from edge extractions. This method is novel and could give crucial insight into how cameras behave in natural scenes, identifying trends in image sharpness. It is clear from both KITTI-360 and Woodscape experiments that distortion directly affects the image quality of natural scenes and differs depending on the scene and camera type. For example, KITTI experiments show largely uniform results due to minimal to no distortion in CaRa evaluation. In contrast, there are clear variations between all three circular regions in fisheye cameras where MTF50 measurements are spread out from each other. It is clear from this work that it is essential to establish the criteria for optical quality measurements in natural scenes. The position of cameras on automotive vehicles can influence the pattern of results obtained from natural scenes. This is clearly shown in the spatial patterns observed in both CaRa and O'SHea evaluations performed in this work. Simulation may be considered for extending experiments for natural scenes. If real-life lenses can be modeled in automotive simulators, it would be possible to easily replace lenses and perform measurements on the same scene. This would be feasible, especially for investigating corner case scenarios in optical quality. Simulation can provide a method of utilizing real-time camera production tests for computer vision in the future.

APPENDIX A
KITTI MTF50

In this section, we show a complete set of results for all four unrectified and rectified KITTI cameras where the spatial domain is divided into a 8×5 heatmap as shown in Figure 20. Take the following examples:

1) regions (2,1), (2,2), (7,1), (7,2), (2,4), (2,5), (7,4) and (7,5) all have the majority of the outer radial segment,
2) regions (2,3) and (7,3) all have the middle segment as the majority,
3) regions (4,2), (5,2), (4,3), (5,3), (4,4) and (5,4) all have the central segment as the majority,

The results for each of the four cameras in all regions are recorded in Table 2.

A. GRAYSCALE CAMERA 1 (G00)

The following observations can be made from Table 2:

1) **Central Regions (6x)** - horizontal edges have higher values than vertical edges in all six segments except for (5,2). Rectified values are higher than unrectified values in all six segments except for vertical edges in regions (4,3) and (4,4).
2) **Middle Regions (16x)** - horizontal edges have higher values than vertical edges in 13 out of 16 regions except for regions: (5,1), (6,1), and (6,5). For horizontal edges, Rectified values are higher than unrectified values in all regions. For vertical edges, rectified values are higher than unrectified values in 14 of 16 regions except for regions (2,3) and (6,5).
3) **Edge Regions (18x)** - horizontal edges have higher values than vertical edges in 17 out of 18 regions except for region (7,1). For horizontal edges, rectified values are higher than unrectified values except in regions (8,3) and (8,5). For vertical edges, there is no clear majority of edges showing a trend.

B. GRAYSCALE CAMERA 2 (G01)

The following observations can be made from Table 2:

1) **Central Regions (6x)** - horizontal edges have higher values than vertical edges in 5 of 6 segments except for region (5,2). Rectified values are higher than unrectified values in all six segments except for vertical edges in the region (4,3).
2) **Middle Regions (16x)** - horizontal edges have higher values than vertical edges in regions: (3,2), (2,3), (3,3), (6,3), (7,3), (3,4), (6,4), (3,5) and (6,5). For both horizontal and vertical edges, rectified values are higher than unrectified values in all 16 segments except for region (2,3).
3) **Edge Regions (18x)** - horizontal edges have higher values than vertical edges in 17 out of 18 regions (except for region (7,1)). For horizontal edges, rectified values are higher than unrectified values except in regions (8,2), (1,3), and (8,3). For vertical edges, unrectified values are higher than rectified values except in regions (7,2), (8,3), (7,4), (8,4), (2,5), and (7,5).

C. COLORED CAMERA 3 (C02)

The following observations can be made from Table 2:

1) **Central Regions (6x)** -horizontal edges have higher values than vertical edges in 4 of 6 segments except for regions (4,2) and (5,2). Rectified values are higher than unrectified values in all six regions.
2) **Middle Regions (16x)** - horizontal edges have lower values than vertical edges in 11 of 16 regions except for (2,3), (3,3), (3,4), (4,5), and (5,5). For horizontal edges,

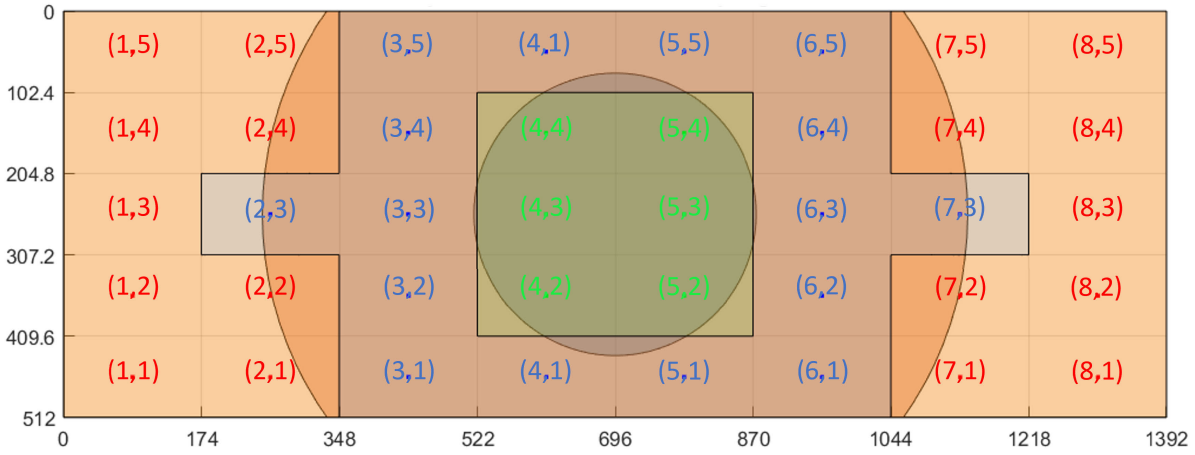

FIGURE 20. O'SHea ROI locations in KITTI.

TABLE 2. NS-SFR MTF50 on all four KITTI cameras for both unrectified(original) and rectified (undistorted) where each row corresponds to a heatmap region in the 8 × 5 heatmap from Figure 20.

Coord.	G00 (H)	G00 (V)	G00 (H*)	G00 (V*)	G01 (H)	G01 (V)	G01 (H*)	G01 (V*)	C02 (H)	C02 (V)	C02 (H*)	C02 (V*)	C03 (H)	C03 (V)	C03 (H*)	C03 (V*)
(4,2)	**0.2413**	0.2290	***0.2946***	***0.2778***	**0.2518**	0.2417	***0.2910***	***0.2890***	0.2112	**0.2201**	***0.2662***	***0.2650***	0.1905	**0.1997**	***0.2368***	***0.2304***
(5,2)	0.2250	**0.2471**	***0.2573***	***0.2781***	0.2256	**0.2330**	***0.2498***	***0.2565***	0.2113	**0.2267**	***0.2491***	***0.2719***	0.1982	**0.2078**	***0.2445***	***0.2392***
(4,3)	**0.2204**	0.2085	***0.2692***	0.1838	**0.2442**	0.2141	***0.2545***	0.1739	**0.2167**	0.1940	***0.2410***	***0.2433***	**0.2067**	0.1829	***0.2378***	***0.1986***
(5,3)	**0.2347**	0.2037	***0.2520***	***0.2324***	**0.2269**	0.1992	***0.2580***	***0.2132***	**0.2171**	0.2140	***0.2391***	***0.2341***	**0.2207**	0.1964	***0.2319***	0.1959
(4,4)	**0.2415**	0.2076	***0.2660***	0.2033	**0.2181**	0.2037	***0.2423***	***0.2148***	**0.2362**	0.1881	***0.2527***	***0.2042***	**0.2166**	0.1777	0.2011	***0.2031***
(5,4)	**0.2265**	0.1999	***0.2813***	***0.2359***	**0.2049**	0.1913	***0.2382***	***0.2128***	**0.2134**	0.2071	***0.2509***	***0.2199***	**0.2130**	0.2025	***0.2435***	***0.2216***
(3,1)	**0.2035**	0.1900	***0.2402***	***0.2165***	0.1965	**0.2110**	***0.2321***	***0.2121***	0.1831	**0.1920**	***0.2256***	***0.2265***	**0.1667**	0.1630	***0.1935***	***0.1792***
(4,1)	**0.1897**	0.1741	***0.2218***	***0.2000***	0.1932	**0.2089**	***0.2197***	***0.2147***	0.1732	**0.2138**	***0.2075***	***0.2318***	0.1622	**0.2290**	***0.2007***	0.2098
(5,1)	0.1798	**0.2165**	***0.2141***	***0.2823***	0.1905	**0.2317**	***0.2220***	***0.2727***	0.1817	**0.2297**	***0.2022***	***0.2641***	0.1604	**0.2139**	***0.2037***	***0.2472***
(6,1)	0.2082	**0.2182**	***0.2447***	***0.2297***	0.2115	**0.2181**	***0.2297***	***0.2499***	0.1980	**0.2288**	***0.2395***	***0.2313***	0.1804	**0.2114**	***0.2212***	***0.2360***
(3,2)	**0.2305**	0.1907	***0.2722***	***0.2154***	**0.2420**	0.2165	***0.2637***	***0.2303***	0.2041	**0.2068**	***0.2430***	***0.2142***	**0.1854**	0.1851	***0.2128***	***0.1969***
(6,2)	**0.2192**	0.2172	***0.2325***	***0.2430***	0.1967	**0.2166**	***0.2295***	***0.2296***	0.2142	**0.2186**	***0.2351***	***0.2284***	0.2091	**0.2115**	***0.2168***	***0.2234***
(2,3)	**0.2236**	0.1695	***0.2440***	0.1672	**0.2277**	0.1850	**0.2053**	0.1793	**0.2115**	0.1919	***0.2163***	***0.2014***	**0.1961**	0.1812	0.1867	***0.1815***
(3,3)	**0.2050**	0.2033	***0.2260***	***0.2051***	**0.2201**	0.2007	***0.2404***	***0.2274***	**0.2136**	0.2021	***0.2291***	***0.2198***	**0.2056**	0.1910	***0.2233***	***0.2133***
(6,3)	**0.2326**	0.2046	***0.2494***	***0.2301***	**0.2324**	0.2233	***0.2629***	***0.2268***	0.2049	**0.2167**	***0.2450***	***0.2518***	0.1969	**0.2217**	***0.2279***	***0.2313***
(7,3)	**0.2481**	0.2055	***0.2518***	***0.2102***	**0.2218**	0.1979	***0.2380***	***0.2279***	0.2125	**0.2190**	***0.2371***	0.2000	**0.1942**	0.1927	***0.2063***	0.1821
(3,4)	**0.2289**	0.1919	***0.2560***	***0.2039***	**0.2459**	0.1793	***0.2624***	***0.1916***	**0.2091**	0.1988	***0.2469***	***0.2223***	**0.2034**	0.1847	***0.2339***	***0.1992***
(6,4)	**0.2232**	0.2103	***0.2408***	***0.2123***	**0.2194**	0.1900	***0.2335***	***0.2420***	0.2179	**0.2278**	***0.2356***	0.2112	**0.2032**	0.2029	***0.2183***	***0.2092***
(3,5)	**0.1975**	0.1917	***0.2604***	***0.2206***	**0.2292**	0.2133	***0.2752***	***0.2427***	0.2144	**0.2281**	***0.2771***	***0.2572***	**0.2070**	0.1953	***0.2346***	***0.2489***
(4,5)	**0.2141**	0.2089	***0.2209***	***0.2214***	0.2071	**0.2074**	***0.2501***	***0.2109***	**0.2138**	0.1952	***0.2707***	***0.2116***	**0.1961**	0.1902	***0.2354***	***0.1932***
(5,5)	**0.2191**	0.2099	***0.2841***	***0.2144***	0.1976	**0.2205**	***0.2154***	***0.2252***	**0.2167**	0.1917	***0.2821***	***0.2307***	0.1844	**0.2139**	***0.2237***	***0.2260***
(6,5)	0.2163	**0.2211**	***0.2637***	0.2139	**0.2231**	0.2092	***0.2640***	***0.2272***	0.2212	**0.2250**	***0.2526***	**0.2150**	0.1990	**0.2107**	***0.2204***	***0.2223***
(1,1)	**0.2116**	0.1538	***0.2392***	0.1391	**0.2010**	0.1466	***0.2299***	0.1402	**0.1968**	0.1791	***0.2249***	0.1641	**0.1680**	0.1647	***0.1817***	0.1377
(2,1)	**0.1934**	0.1652	***0.2282***	***0.1666***	**0.2123**	0.1772	***0.2371***	0.1747	**0.1968**	0.1836	***0.2103***	***0.1902***	**0.1710**	0.1706	***0.1829***	0.1617
(7,1)	0.2047	**0.2175**	***0.2213***	***0.2187***	0.2016	**0.2076**	***0.2562***	0.1969	0.1938	**0.1950**	***0.2329***	***0.1955***	0.1864	**0.1990**	***0.2289***	0.1942
(8,1)	**0.2136**	0.2069	***0.2381***	0.1818	**0.2240**	0.1845	***0.2309***	0.1643	**0.2061**	0.1837	***0.2208***	0.1771	**0.2132**	0.1760	0.2066	0.1409
(1,2)	**0.2340**	0.1487	***0.2664***	0.1417	**0.2293**	0.1519	***0.2403***	0.1443	**0.2246**	0.1854	***0.2520***	0.1615	**0.1888**	0.1681	***0.2008***	0.1430
(2,2)	**0.2265**	0.1591	***0.2585***	***0.1620***	**0.2252**	0.1766	***0.2669***	0.1685	**0.2164**	0.1919	***0.2493***	**0.1894**	0.1799	0.1747	***0.2142***	0.1698
(7,2)	**0.2284**	0.2036	***0.2426***	***0.2123***	**0.2269**	0.1931	***0.2534***	***0.1983***	**0.2102**	0.2049	***0.2160***	0.1981	**0.2142**	0.2056	0.2036	0.1860
(8,2)	**0.2207**	0.1921	***0.2342***	***0.1924***	**0.2272**	0.1872	**0.2259**	0.1841	**0.2111**	0.2059	***0.2181***	0.1751	**0.1945**	0.1798	0.1889	0.1533
(1,3)	**0.2081**	0.1605	***0.2205***	0.1422	**0.2394**	0.1631	**0.2286**	0.1495	**0.1959**	0.1944	***0.2220***	0.1702	**0.1931**	0.1753	***0.1999***	0.1556
(8,3)	**0.2393**	0.1891	0.2348	0.1804	**0.2481**	0.1745	0.2295	***0.1777***	**0.2197**	0.1977	0.2099	0.1733	**0.1943**	0.1674	0.1897	0.1449
(1,4)	**0.2319**	0.1564	***0.2586***	0.1411	**0.2331**	0.1603	***0.2608***	0.1465	**0.2257**	0.1957	***0.2527***	0.1790	**0.2056**	0.1702	***0.2125***	0.1567
(2,4)	**0.2250**	0.1663	***0.2558***	0.1611	**0.2349**	0.1745	***0.2773***	0.1714	**0.2238**	0.1997	***0.2544***	0.1987	**0.2066**	0.1838	***0.2338***	0.1831
(7,4)	**0.2240**	0.1940	***0.2558***	***0.2219***	**0.1997**	0.1995	***0.2329***	***0.2153***	0.2092	**0.2105**	***0.2419***	0.1993	0.1921	0.1921	***0.2062***	0.1725
(8,4)	**0.2152**	0.1616	***0.2640***	***0.2010***	**0.2327**	0.1775	***0.2845***	***0.1908***	**0.2199**	0.1953	***0.2341***	0.1653	**0.2037**	0.1699	***0.2045***	0.1448
(1,5)	**0.2060**	0.1525	***0.2399***	0.1371	**0.2280**	0.1436	***0.2451***	0.1420	**0.2089**	0.1934	***0.2267***	0.1672	**0.1926**	0.1671	***0.1937***	0.1543
(2,5)	**0.2176**	0.1701	***0.2285***	***0.1767***	**0.2339**	0.1866	***0.2550***	***0.2063***	**0.2198**	0.2108	***0.2450***	***0.2145***	**0.1922**	0.1852	***0.2135***	***0.1928***
(7,5)	**0.2174**	0.2009	***0.2821***	***0.2361***	**0.2228**	0.1944	***0.2365***	***0.2150***	**0.2274**	0.2150	***0.2494***	**0.2118**	**0.2001**	0.1917	***0.2098***	0.1649
(8,5)	**0.2626**	0.1614	0.2369	0.1542	**0.2229**	0.1691	***0.2465***	0.1639	**0.2523**	0.1889	0.2140	0.1686	**0.1918**	0.1645	***0.1928***	0.1390

Note: G0X = Grayscale camera X where (X = 0,1), C0X = Colored camera X where (X = 2,3), H = horizontal MTF50 (unrectified), V = vertical MTF50 (unrectified),H* = horizontal MTF50 (rectified), V* = vertical MTF50 (rectified), **Bold** = highest unrectified, ***Bold italicized*** = rectified > unrectified, Underlined = unrectified > rectified.

rectified values are higher than unrectified values in all regions. For vertical edges, rectified values are higher than unrectified values except for regions (7,3), (6,4), and (6,5).

3) **Edge Regions (18x)** - horizontal edges have higher values than vertical edges in 16 out of 18 regions except for regions (7,1) and (7,4). For horizontal edges, rectified values are higher than unrectified values except in regions (8,3) and (8,5). For vertical edges, unrectified values are higher than rectified values except in regions (2,1), (7,1), and (2,5).

D. COLORED CAMERA 4 (C03)

The following observations can be made from Table 2:

1) **Central Regions (6x)** - horizontal edges have higher values than vertical edges in 4 of 6 segments except for regions (4,2) and (5,2). For horizontal edges, rectified values are higher than unrectified values except in

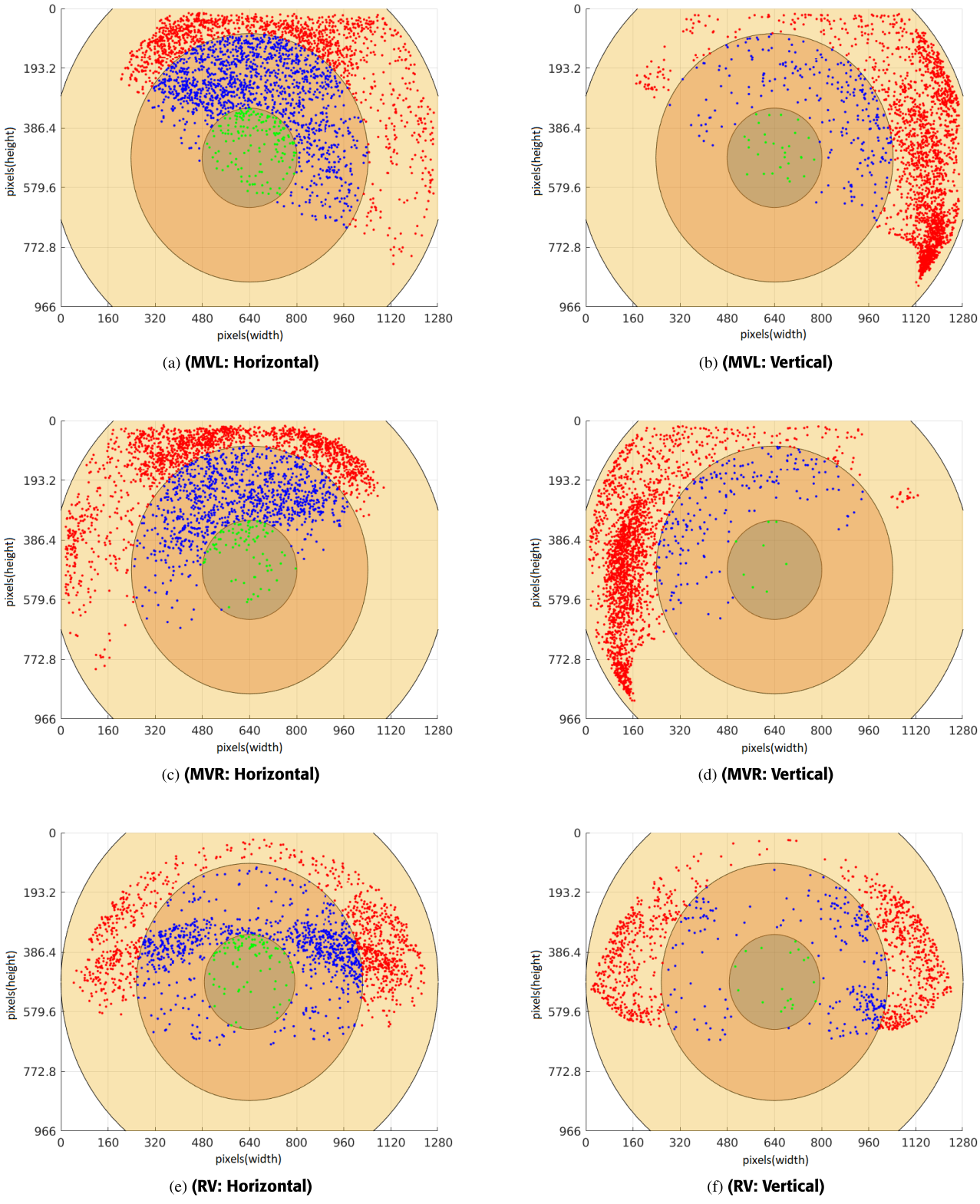

(a) **(MVL: Horizontal)** (b) **(MVL: Vertical)**

(c) **(MVR: Horizontal)** (d) **(MVR: Vertical)**

(e) **(RV: Horizontal)** (f) **(RV: Vertical)**

FIGURE 21. **The Spatial Distribution of Woodscape for MVL, MVR, and RV views (ST=0.02, esfW=5). First column: horizontal edges, Second column: vertical edges.**

region (4,4). For vertical edges, rectified values are higher than unrectified values except in region (5,3).

2) **Middle Regions (16x)** - horizontal edges have higher values than vertical edges in 9 of 16 regions except

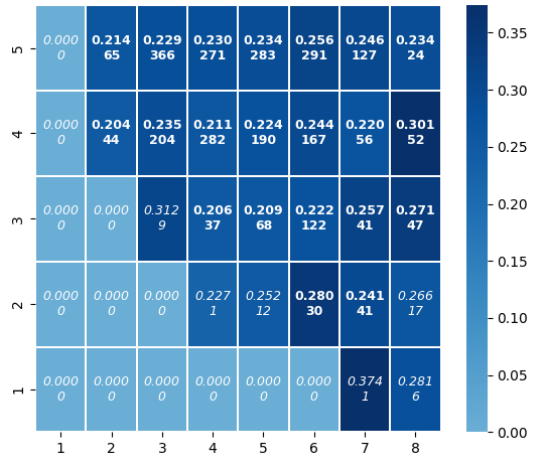

(a) **(MVL: Horizontal)**

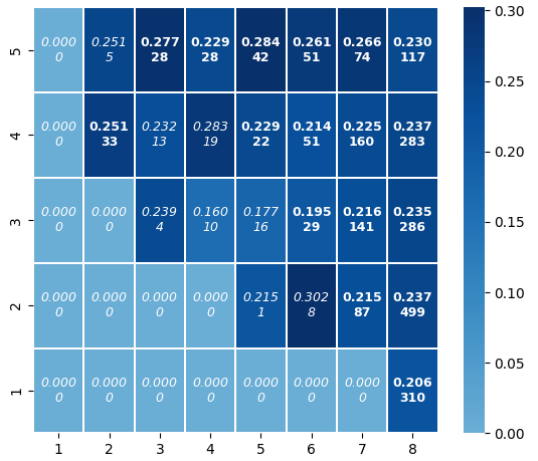

(b) **(MVL: Vertical)**

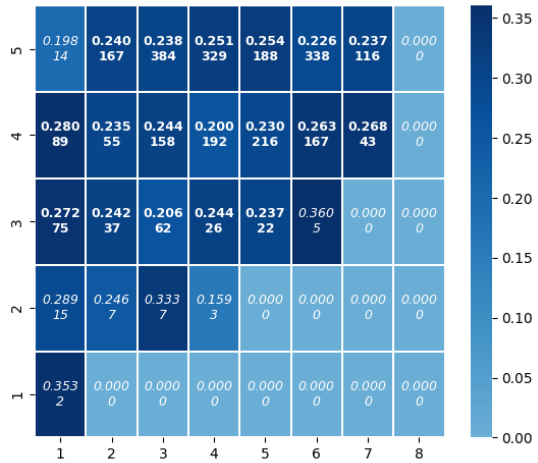

(c) **(MVR: Horizontal)**

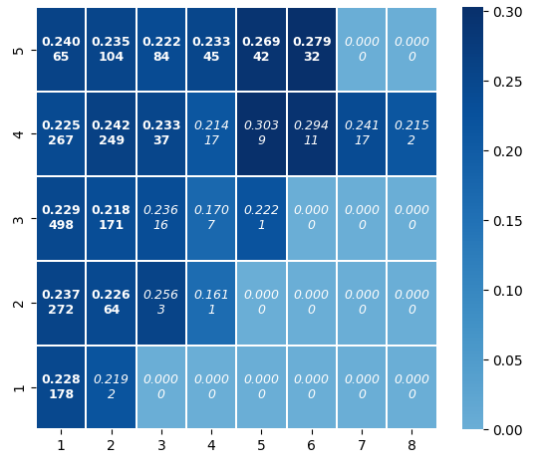

(d) **(MVR: Vertical)**

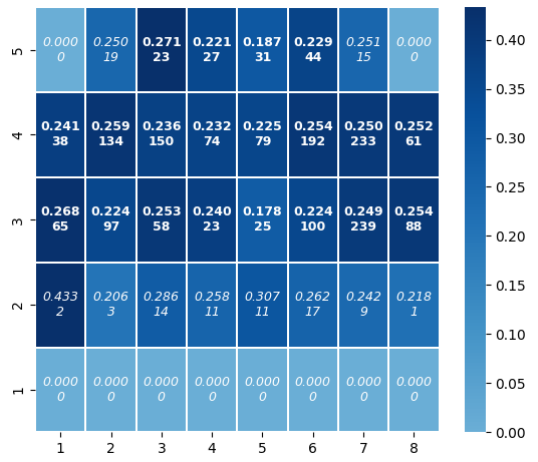

(e) **(RV: Horizontal)**

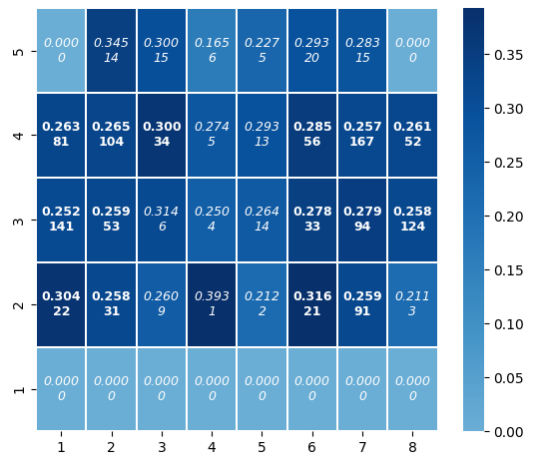

(f) **(RV: Vertical)**

FIGURE 22. O'SHea MTF50 Analysis of the Spatial Domain in Woodscape for MVL, MVR, and RV views (ST=0.02, esfW=5). Each region displays the mean MTF50 and the number of data points found where <20 samples are shown in italics.

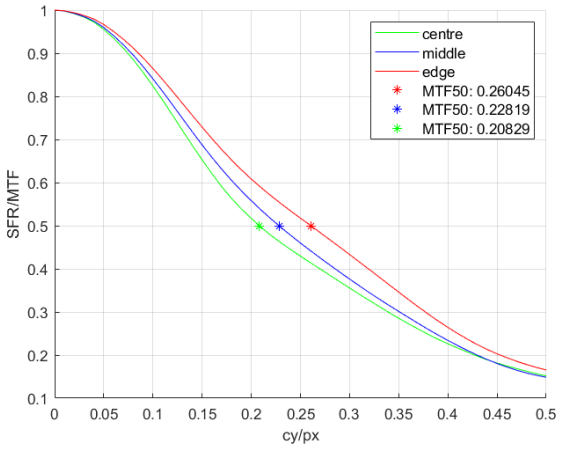

(a) **(MVL: Horizontal)**

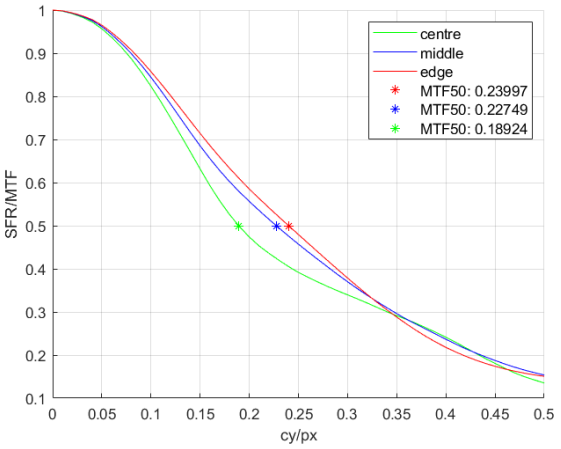

(b) **(MVL: Vertical)**

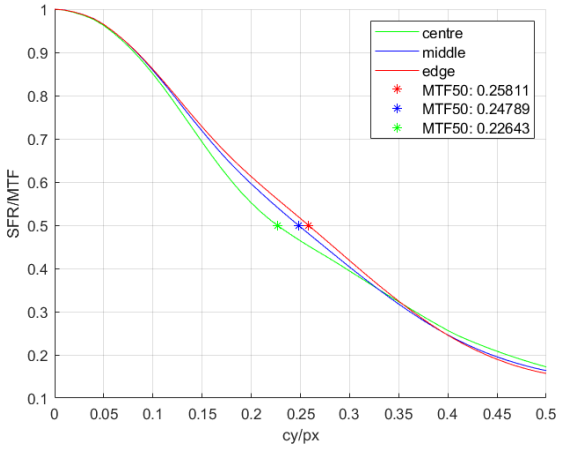

(c) **(MVR: Horizontal)**

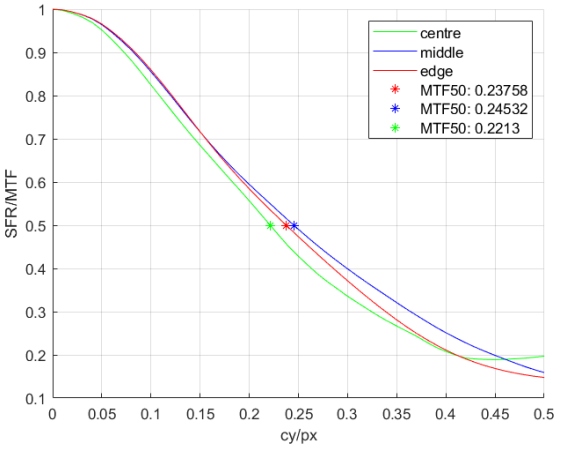

(d) **(MVR: Vertical)**

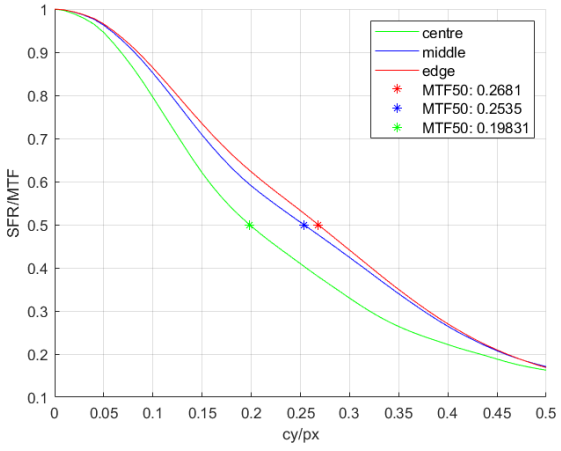

(e) **(RV: Horizontal)**

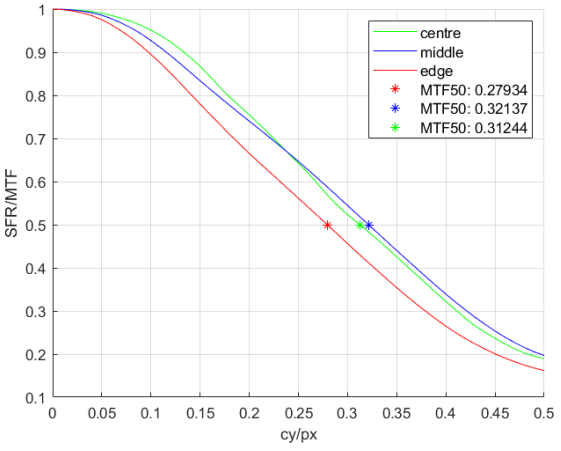

(f) **(RV: Vertical)**

FIGURE 23. **MTF plots of Woodscape for MVL, MVR, and RV views (ST=0.02, esfW=5). First column: horizontal edges, Second column: vertical edges.**

for regions (4,1), (5,1), (6,1), (6,2), (6,3), (5,5) and (6,5). For horizontal edges, rectified values are higher than unrectified values except in region (2,3). For vertical edges, rectified values are higher than unrectified values except in regions (4,1) and (7,3).

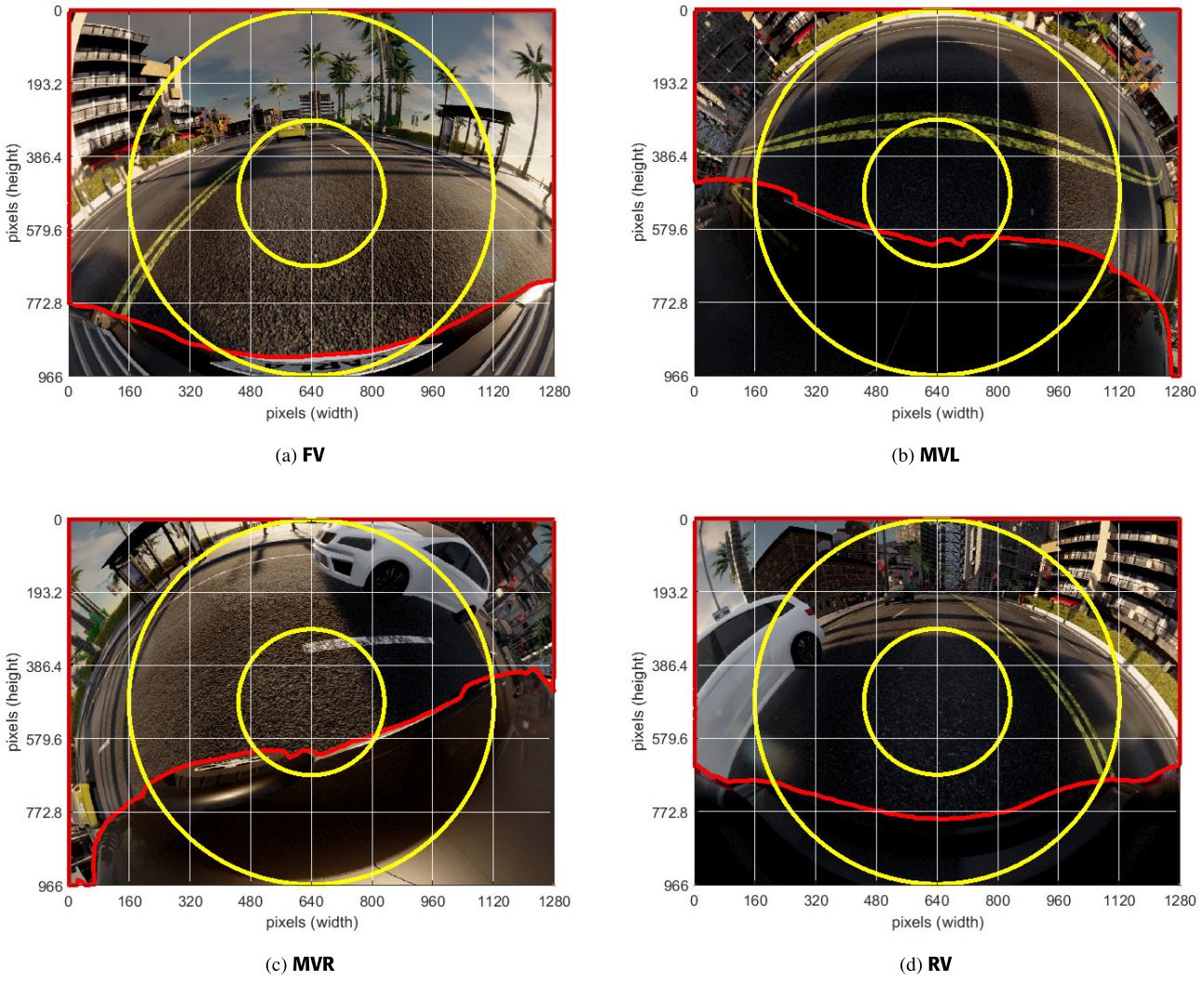

(a) **FV** (b) **MVL**

(c) **MVR** (d) **RV**

FIGURE 24. **RMLA and CaRa on all four perspectives of SynWoodscape. Note: the Camera Radial Distances are aligned with the periphery of the fisheye camera and any edge categorized would be representative of the actual lens location.**

3) **Edge Regions (18x)** - horizontal edges have higher values than vertical edges except for regions (7,1), (7,4). For horizontal edges, rectified values are higher than unrectified values except in regions (8,1), (7,2), (8,2), and (8,3). For vertical edges, unrectified values are higher than rectified values except in region (2,5).

APPENDIX B
WOODSCAPE

This section contains additional results for Woodscape MTF50 MVL, MVR, and RV camera perspectives. Figure 21 illustrates different patterns of MTF50 spatial distributions in the camera perspectives. For example, the outline of road markings and pavement features in the road for MVL and MVR in Figures 21a and 21c have clustered points in the top central background (see Figures 4b and 4c for comparison). Similarly, for vertical edges, most can be found along the periphery at the bottom left or right foregrounds of the images (see Figures 21b and 21d) and compare to the same regions pixel regions in Figures 4b and 4c. Finally, the RV camera perspective illustrates a similar pattern of behavior to the FV perspective, where the outline of the road contains tightly clustered points for horizontal edges, whereas most of the edges for vertical edges can be found at the periphery of the camera (i.e., located on the buildings above the ground). Furthermore, the degree of visibility for the RV perspective is much smaller due to the greater presence of vignetting in the camera lenses(visible in Figure 4a). This ultimately leads to less CaRa being isolated in the particular regions of interest. The spatial distributions are accompanied by their respective O'SHea and CaRa evaluations in Figures 22 and 23, respectively. Noticeably, all MTF50 measurements can be located within the range of 0.22-0.32cy/px illustrating that it is possible to extract optical quality results from any Woodscape perspective.

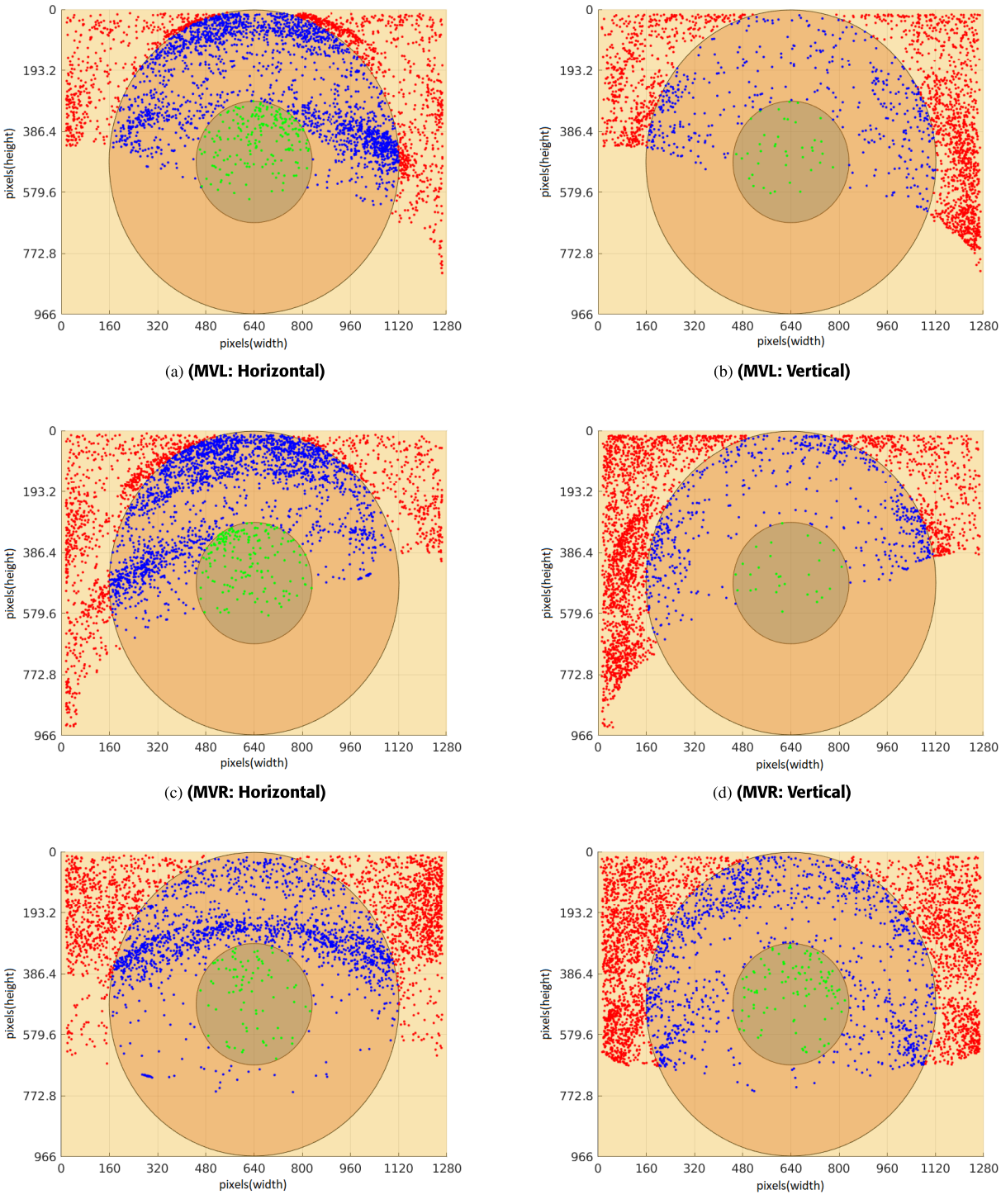

(a) **(MVL: Horizontal)** (b) **(MVL: Vertical)**

(c) **(MVR: Horizontal)** (d) **(MVR: Vertical)**

(e) **(RV: Horizontal)** (f) **(RV: Vertical)**

FIGURE 25. The Spatial Distribution of Woodscape for MVL, MVR and RV views (ST=0.02, esfW=5). First column: horizontal edges, Second column: vertical edges.

APPENDIX C
SYNWOODSCAPE

This section contains additional results for SynWoodscape MTF50 MVL, MVR, and RV camera perspectives. Figure 25 illustrates different patterns of MTF50 spatial distributions in the camera perspectives. As a comparison to Woodscape, the spatial distributions are completely different in shape. However, the locations of the clustered data points are similar to that of Woodscape (see Figure 21). For example, the outline of road markings and pavement features in the road

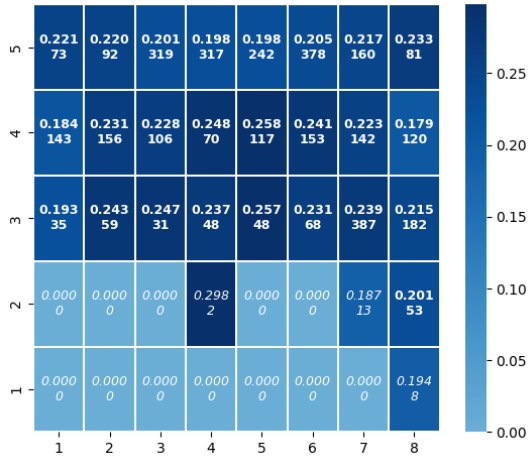

(a) **(MVL: Horizontal)**

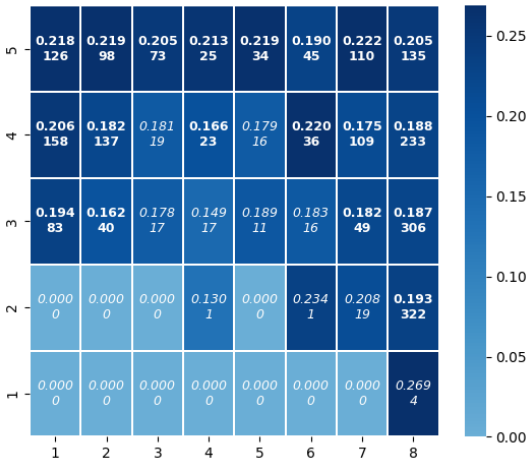

(b) **(MVL: Vertical)**

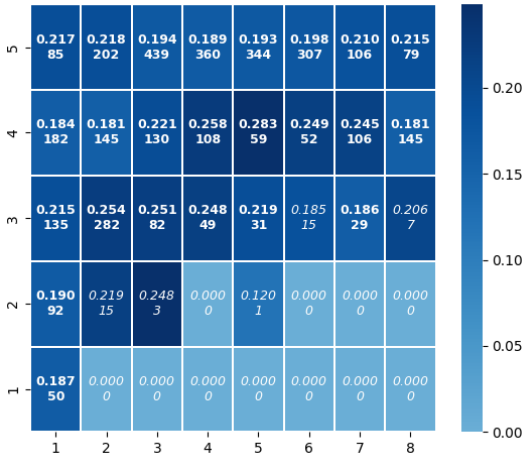

(c) **(MVR: Horizontal)**

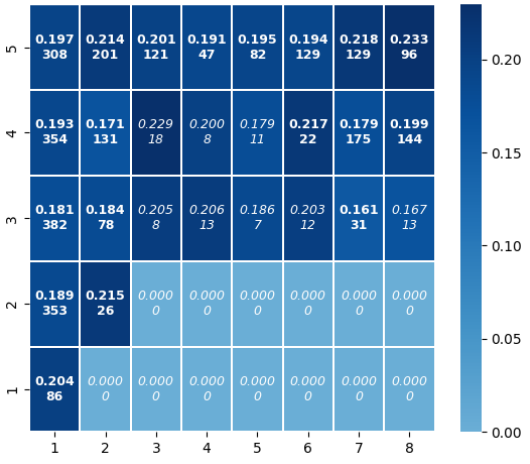

(d) **(MVR: Vertical)**

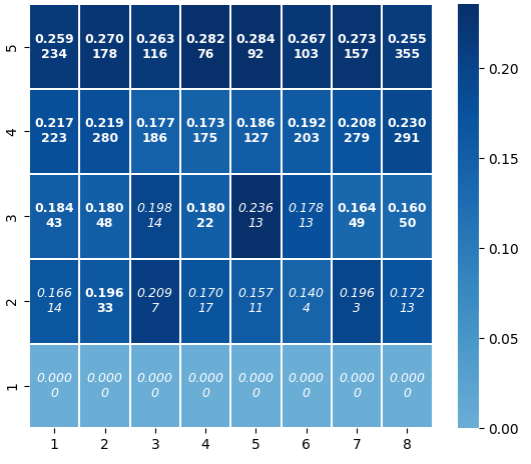

(e) **(RV: Horizontal)**

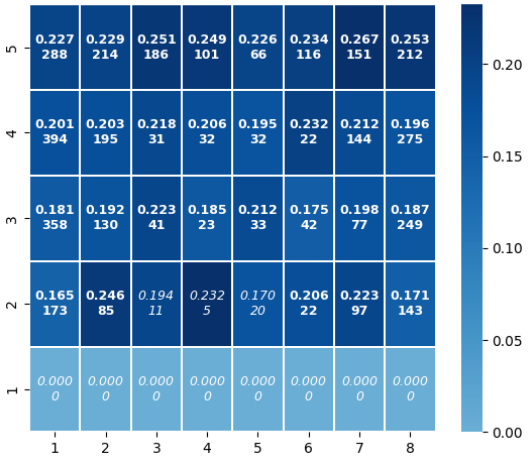

(f) **(RV: Vertical)**

FIGURE 26. O'SHea MTF50 Analysis of the Spatial Domain in SynWoodscape for MVL, MVR, and RV views (ST=0.02, esfW=5). Each region displays the mean MTF50 and the number of data points found where <20 samples are shown in italics.

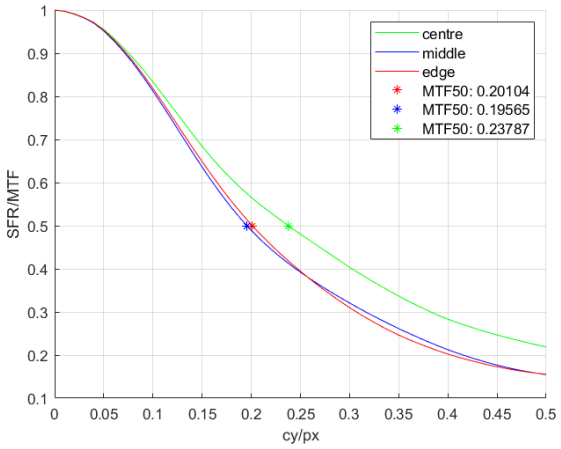

(a) **(MVL: Horizontal)**

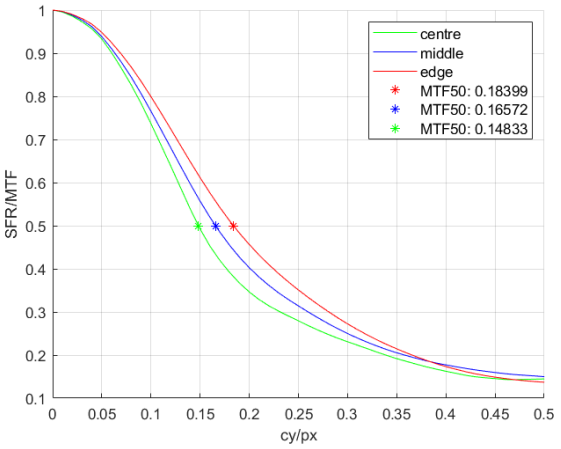

(b) **(MVL: Vertical)**

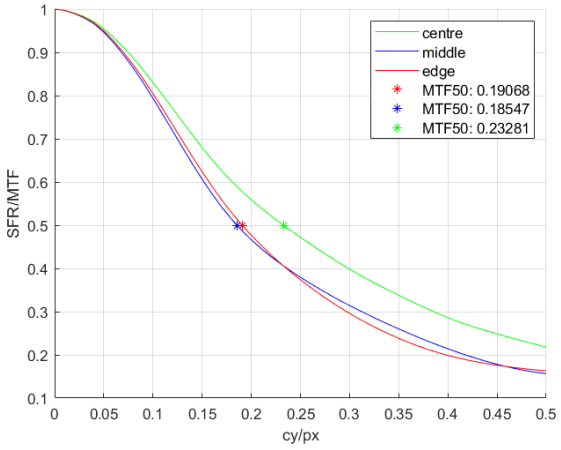

(c) **(MVR: Horizontal)**

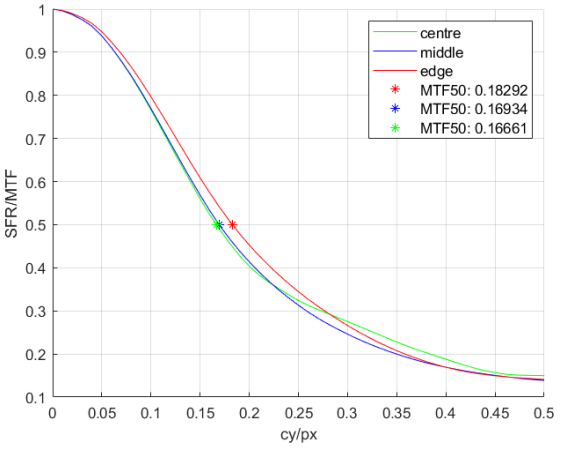

(d) **(MVR: Vertical)**

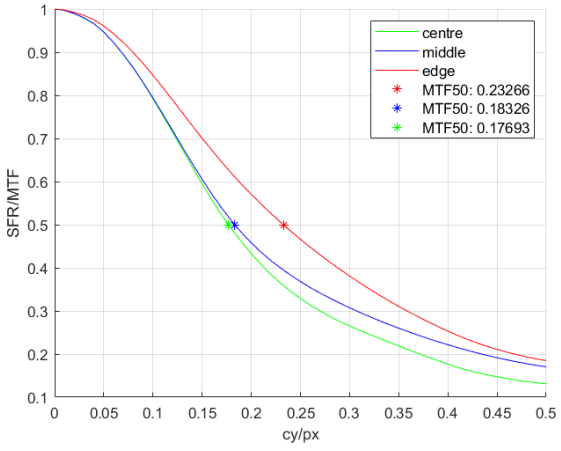

(e) **(RV: Horizontal)**

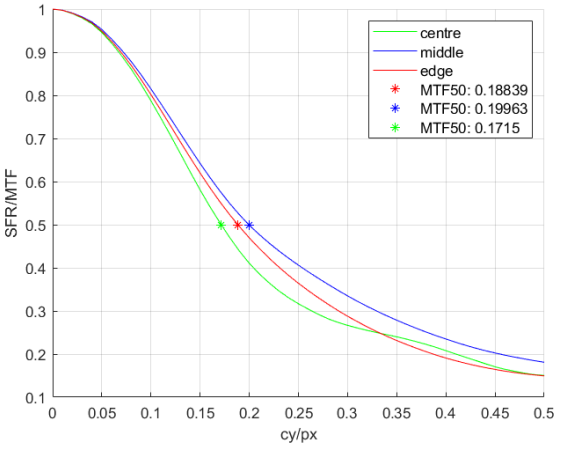

(f) **(RV: Vertical)**

FIGURE 27. **MTF plots of SynWoodscape for MVL, MVR, and RV views (ST=0.02, esfW=5). First column: horizontal edges, Second column: vertical edges.**

for MVL and MVR in Figures 25a and 25c have clustered points in the top central background (see Figures 24b and 24c for comparison). Similarly, for vertical edges, most can be found along the periphery at the bottom left or right

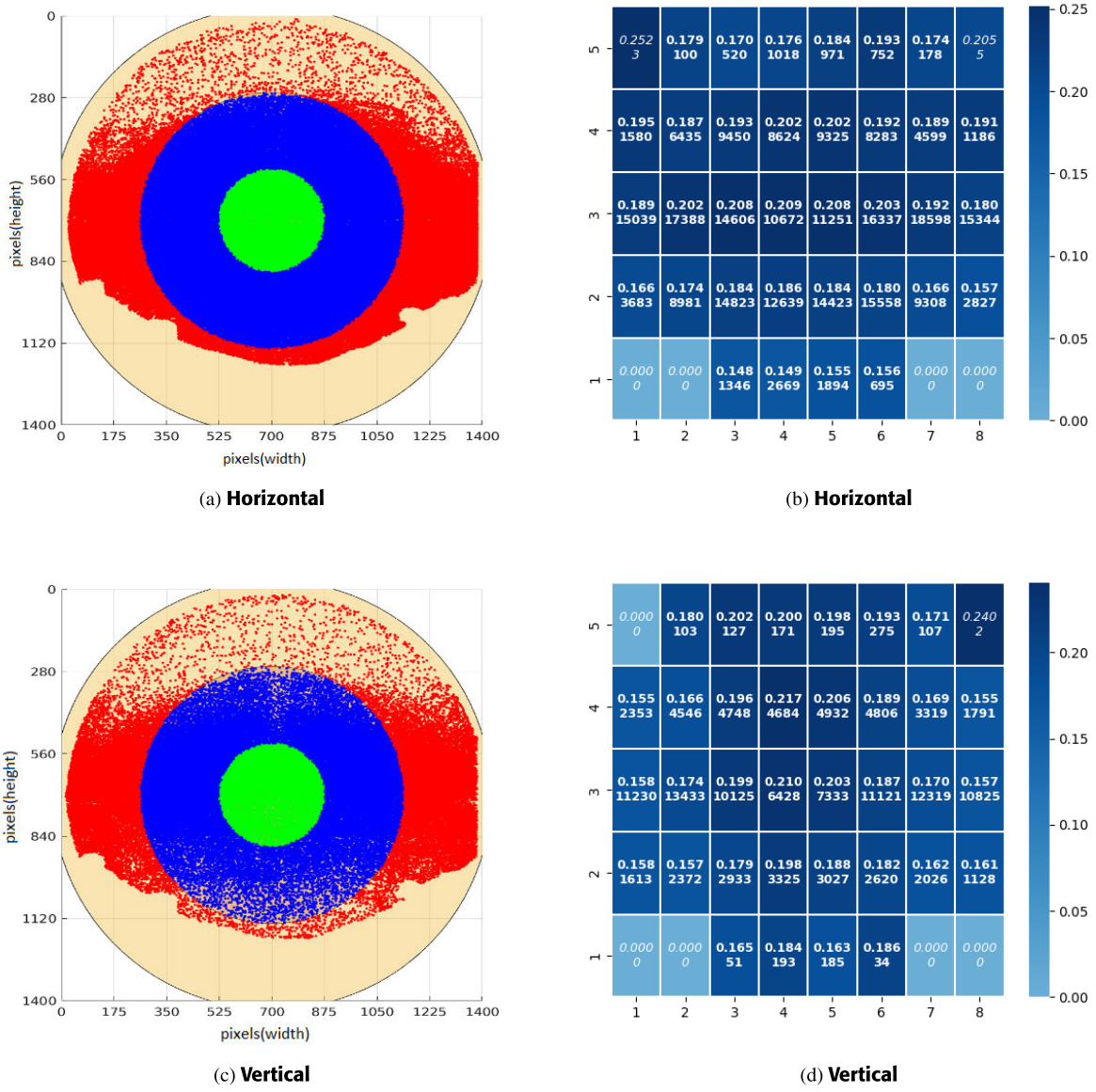

(a) **Horizontal** (b) **Horizontal**

(c) **Vertical** (d) **Vertical**

FIGURE 28. KITTI-360 Spatial Distribution and O'SHea MTF50 Analysis for BSISO12233:2023 [21] on the right camera with NS-SFR parameters of (ST=0.02, esfW=5). Note: Colours represent the spatial domain location according to CaRa (see Section V-B Figure 11a and Figure 12 for left camera results), i.e., center (green), middle(blue) and edge(red). Each region displays the mean MTF50, and the number of data points found where <20 samples are shown in italics.

foregrounds of the images (see Figures 25b and 25d) and compare to the same regions pixel regions in Figures 24b and 24c). Finally, the RV camera perspective illustrates a similar pattern of behavior to the FV perspective, where the outline of the road contains tightly clustered points for horizontal edges, whereas most of the edges for vertical edges can be found at the periphery of the camera (i.e., located on the buildings above the ground). Furthermore, the degree of visibility for the RV perspective is much smaller due to the greater presence of vignetting in the camera lenses(visible in Figure 24a). This ultimately leads to less CaRa being isolated in the particular regions of interest. The spatial distributions are accompanied by their respective O'SHea and CaRa evaluations in Figures 26 and 27, respectively. Noticeably, all MTF50 measurements can be located within the range of 0.22-0.32cy/px illustrating that it is possible to extract optical quality results from any Woodscape perspective.

ACKNOWLEDGMENT

The authors would like to thank Dr. Oliver van Zwanenberg for his invaluable support in integrating the latest version of the Slanted Edge Method (ISO12233:2023) into this study.

REFERENCES

[1] I. LLC. (2023). *Documentation—V23.1–Pre-Distorted and Special Charts for Fisheye Lenses | Imatest*. [Online]. Available: https://www.imatest.com/support/docs/23-1/pre-distorted-charts/

[2] C. Eising, J. Horgan, and S. Yogamani, "Near-field perception for low-speed vehicle automation using surround-view fisheye cameras," *IEEE Trans. Intell. Transp. Syst.*, vol. 23, no. 9, pp. 13976–13993, Sep. 2022.

[3] C. Krebs, P. Müller, and A. Braun, "Impact of windshield optical aberrations on visual range camera based classification tasks performed by CNNs," in *London Imaging Meeting*, vol. 2. Springfield, VA, USA: Society for Imaging Science and Technology, 2021, pp. 83–87.

[4] D. W. Wolf, M. Ulrich, and A. Braun, "Windscreen optical quality for AI algorithms: Refractive power and MTF not sufficient," 2023, *arXiv:2305.14513*.

[5] P. Müller, M. Brummel, and A. Braun, "Spatial recall index for machine learning algorithms," in *London Imaging Meeting*, vol. 2021, no. 1. Oxford, U.K.: Ingenta Connect, 2021, pp. 58–62.

[6] M. Brummel, P. Müller, and A. Braun, "Spatial precision and recall indices to assess the performance of instance segmentation algorithms," *Electron. Imag.*, vol. 34, no. 16, pp. 101-1–101-6, Jan. 2022.

[7] P. Müller, A. Braun, and M. Keuper, "Classification robustness to common optical aberrations," in *Proc. IEEE/CVF Int. Conf. Comput. Vis. Workshops (ICCVW)*, Oct. 2023, pp. 3632–3643.

[8] S. Dodge and L. Karam, "Understanding how image quality affects deep neural networks," in *Proc. 8th Int. Conf. Quality Multimedia Exper. (QoMEX)*, Jun. 2016, pp. 1–6.

[9] D. Jakab, B. M. Deegan, S. Sharma, E. M. Grua, J. Horgan, E. Ward, P. van de Ven, A. Scanlan, and C. Eising, "Surround-view fisheye optics in computer vision and simulation: Survey and challenges," *IEEE Trans. Intell. Transp. Syst.*, vol. 25, no. 9, pp. 10542–10563, Sep. 2024.

[10] O. van Zwanenberg, "Camera spatial frequency response derived from pictorial natural scenes," Ph.D. dissertation, School Comput. Sci. Eng., Univ. Westminster, London, U.K., 2022.

[11] O. Van Zwanenberg, S. Triantaphillidou, R. Jenkin, and A. Psarrou, "Natural scene derived camera edge spatial frequency response for autonomous vision systems," in *IS&T/IoP London Imaging Meeting 2021*. Springfield, VA, USA: Society of Imaging Science and Technology, 2021.

[12] O. Van Zwanenberg, S. Triantaphillidou, and R. Jenkin, "A tool for deriving camera spatial frequency response from natural scenes (NS-SFR)," in *Proc. Electron. Imag., Image Quality Syst. Perform. (XX)*, Jan. 2023, pp. 1–6.

[13] O. van Zwanenberg, S. Triantaphillidou, R. Jenkin, and A. Psarrou, "Edge detection techniques for quantifying spatial imaging system performance and image quality," in *Proc. IEEE/CVF Conf. Comput. Vis. Pattern Recognit. Workshops (CVPRW)*, Jun. 2019, pp. 1871–1879.

[14] O. van Zwanenberg, S. Triantaphillidou, R. B. Jenkin, and A. Psarrou, "Estimation of ISO12233 edge spatial frequency response from natural scene derived step-edge data," *J. Imag. Sci. Technol.*, vol. 65, no. 6, Nov. 2021, Art. no. 060402.

[15] *Photography—Electronic Still Picture Imaging—Resolution and Spatial Frequency Responses*, Standard BS ISO 12233:2017, BSI Standards Publication, 2017.

[16] P. D. Burns and D. Williams, "Camera resolution and distortion: Advanced edge fitting," *Electron. Imag.*, vol. 30, no. 12, pp. 171-1–171-5, Jan. 2018.

[17] D. Jakab, E. M. Grua, B. M. Deegan, A. Scanlan, P. Van De Ven, and C. Eising, "Measuring natural scenes SFR of automotive fisheye cameras," *Electron. Imag.*, vol. 36, no. 17, pp. 109-1–109-6, Jan. 2024.

[18] A. Geiger, P. Lenz, C. Stiller, and R. Urtasun, "Vision meets robotics: The KITTI dataset," *Int. J. Robot. Res.*, vol. 32, no. 11, pp. 1231–1237, Sep. 2013.

[19] Y. Liao, J. Xie, and A. Geiger, "KITTI-360: A novel dataset and benchmarks for urban scene understanding in 2D and 3D," *IEEE Trans. Pattern Anal. Mach. Intell.*, vol. 45, no. 3, pp. 3292–3310, Mar. 2023.

[20] S. Yogamani, C. Hughes, J. Horgan, G. Sistu, S. Chennupati, M. Uricar, S. Milz, M. Simon, K. Amende, C. Witt, H. Rashed, S. Nayak, S. Mansoor, P. Varley, X. Perrotton, D. Odea, and P. Pérez, "WoodScape: A multi-task, multi-camera fisheye dataset for autonomous driving," in *Proc. IEEE/CVF Int. Conf. Comput. Vis. (ICCV)*, Oct. 2019, pp. 9307–9317.

[21] *Photography—Electronic Still Picture Imaging—Resolution and Spatial Frequency Responses*, Standard BS ISO 12233:2023, BSI Standards Publication, 2023.

[22] A. Eichenseer and A. Kaup, "A data set providing synthetic and real-world fisheye video sequences," in *Proc. IEEE Int. Conf. Acoust., Speech Signal Process. (ICASSP)*, Mar. 2016, pp. 1541–1545.

[23] A. R. Sekkat, Y. Dupuis, V. R. Kumar, H. Rashed, S. Yogamani, P. Vasseur, and P. Honeine, "SynWoodScape: Synthetic surround-view fisheye camera dataset for autonomous driving," *IEEE Robot. Autom. Lett.*, vol. 7, no. 3, pp. 8502–8509, Jul. 2022.

[24] A. Dosovitskiy, G. Ros, F. Codevilla, A. Lopez, and V. Koltun, "CARLA: An open urban driving simulator," in *Proc. 1st Annu. Conf. Robot Learn.*, vol. 78, S. Levine, V. Vanhoucke, and K. Goldberg, Eds. Nov. 2017, pp. 1–16.

[25] A. Braun, "Automotive mass production of camera systems: Linking image quality to AI performance," *Tm Technisches Messen*, vol. 90, no. 3, pp. 205–218, Mar. 2023.

[26] B. D. Imaging. *Spatial Frequency Response (SFR): SFRmat*. Accessed: Sep. 23, 2023. [Online]. Available: http://burnsdigitalimaging.com/software/sfrmat/

[27] H. S. N. da Silva, F. B. L. Eick, and A. J. Damião, "Slanted edge method for MTF measurements in the infrared," *Infr. Phys. Technol.*, vol. 118, Nov. 2021, Art. no. 103877.

[28] P. D. Burns, K. Masaoka, K. Parulski, and D. Wueller, "Updated camera spatial frequency response for ISO 12233," *Electron. Imag.*, vol. 34, no. 9, pp. 357-1–357-6, Jan. 2022.

[29] E. W. Fry, S. Triantaphillidou, R. B. Jenkin, J. R. Jarvis, and R. E. Jacobson, "Validation of modulation transfer functions and noise power spectra from natural scenes," *J. Imag. Sci. Technol*, vol. 6, no. 3, 2019, Art. no. 060406.

[30] R. Branca, S. Triantaphillidou, and P. Burns, "Texture MTF from images of natural scenes," *Electron. Imag.*, vol. 29, no. 12, pp. 113–120, Jan. 2017.

[31] A. S. Inc. (2005). *Adobe RGB (1998) Color Image Encoding*. [Online]. Available: https://www.adobe.com/digitalimag/pdfs/AdobeRGB1998.pdf

[32] *Colour Management—Default RGB Colour Space SRGB*, Standard IEC 61966-2-1:1999, I. E. Commission, 1999, p. 13.

[33] J. Canny, "A computational approach to edge detection," *IEEE Trans. Pattern Anal. Mach. Intell.*, vol. PAMI-8, no. 6, pp. 679–698, Nov. 1986.

[34] P. D. Burns, D. Williams, J. Griffith, H. Hall, and S. Cahall, "Application of ISO standard methods to optical design for image capture," *Electron. Imag.*, vol. 32, no. 9, pp. 240-1–240-7, Jan. 2020.

[35] P. Mueller, M. Lehmann, and A. Braun, "Simulating tests to test simulation," *Electron. Imag.*, vol. 32, no. 16, pp. 149-1–149-8, Jan. 2020.

[36] V. F. Zernike, "Beugungstheorie des schneidenver-fahrens und seiner verbesserten form, der phasenkontrastmethode," *Physica*, vol. 1, nos. 7–12, pp. 689–704, May 1934.

[37] I. LLC. (2023). *Documentation—V23.1—MTF Curves and Image Appearance*. [Online]. Available: https://www.imatest.com/support/docs/23-1/mtf_appearance/

[38] C. Hogan and G. Sistu, "Automatic vehicle ego body extraction for reducing false detections in automated driving applications," in *Proc. Irish Conf. Artif. Intell. Cogn. Sci.* Cham, Switzerland: Springer, 2022, pp. 264–275.

[39] M. R2024a. (2024). *Drawfreehand*. [Online]. Available: https://uk.mathworks.com/help/images/ref/drawfreehand.html

[40] I. LLC. (2024). *Documentation Current v24.1—Nyquist Frequency, Aliasing, and Color Moire*. [Online]. Available: https://www.imatest.com/docs/nyquist-aliasing/

[41] V. R. Kumar, C. Eising, C. Witt, and S. K. Yogamani, "Surround-view fisheye camera perception for automated driving: Overview, survey & challenges," *IEEE Trans. Intell. Transp. Syst.*, vol. 24, no. 4, pp. 3638–3659, Apr. 2023.

[42] P. Müller and A. Braun, "Simulating optical properties to access novel metrological parameter ranges and the impact of different model approximations," in *Proc. IEEE Int. Workshop Metrology Automot. (MetroAutomotive)*, Jul. 2022, pp. 133–138.

[43] F. Yu, H. Chen, X. Wang, W. Xian, Y. Chen, F. Liu, V. Madhavan, and T. Darrell, "BDD100K: A diverse driving dataset for heterogeneous multitask learning," in *Proc. IEEE/CVF Conf. Comput. Vis. Pattern Recognit. (CVPR)*, Jun. 2020, pp. 2633–2642.

[44] P. Müller and A. Braun, "MTF as a performance indicator for AI algorithms?" *Electron. Imag.*, vol. 35, no. 16, pp. 125-1–125-7, Jan. 2023.

[45] N. Koren and L. Imatest, "Image information metrics and applications: Reference," Imatest LLC, Boulder, CO, USA, Tech. Rep., Dec. 2023.

[46] B. W. Keelan, "Imaging applications of noise equivalent quanta," *Electron. Imag.*, vol. 28, no. 13, pp. 1–7, Feb. 2016.

[47] N. L. Koren, "Image information metrics from slanted edges: A toolkit of metrics to aid object recognition, machine vision, and artificial intelligence systems," *Electron. Imag.*, vol. 36, no. 9, pp. 256-1–256-17, Jan. 2024.
[48] O. Skorka and P. J. Kane, "Object detection using an ideal observer model," *Electron. Imag.*, vol. 32, no. 16, pp. 41-1–41-7, Jan. 2020.
[49] P. J. Kane, "Signal detection theory and automotive imaging," *Electron. Imag.*, vol. 31, no. 15, pp. 27-1–27-8, Jan. 2019.

DANIEL JAKAB received the M.E. degree in electronic and computer engineering from the University of Limerick, Ireland, in 2022, where he is currently pursuing the Ph.D. degree with the Department of Electronic and Computer Engineering. He worked for nine months in an internship with Black Box R&D, between 2019 and 2020. His Ph.D. work is under the sponsorship of the Lero Science Foundation Ireland-Funded Project, "Treating fisheye cameras natively using CNNs to improve production tolerances of cameras."

EOIN MARTINO GRUA was born in Cork, Ireland, in 1993. He received the B.S. degree in liberal arts and sciences from Amsterdam University College, Amsterdam, The Netherlands, in 2015, the M.S. degree in computer science from Swansea University, Swansea, Wales, in 2016, and the Ph.D. degree in computer science from Vrije Universiteit Amsterdam, Amsterdam, in 2021. In 2021, he was a Research Assistant with the University of Limerick, Limerick, Ireland, where he is currently an Assistant Professor with the Department of Electronic and Computer Engineering. His research interests include artificial intelligence, software engineering and architecture, and sustainability.

REENU MOHANDAS (Member, IEEE) received the M.Tech. degree in digital image computing from the University of Kerala, India, in 2014, the M.Sc. degree in artificial intelligence from CIT, currently Munster Technological University, Cork, Ireland, in 2019, and the Ph.D. degree from the Department of Electronic and Computer Engineering (ECE), University of Limerick, Ireland. She is currently a Research Assistant. Her research interests include computer vision, deep learning, visual cognition applications, VQA models, and edge deployment of deep learning algorithms.

BRIAN MICHAEL DEEGAN (Member, IEEE) received the bachelor's degree in computer engineering and the M.Sc. degree in biomedical engineering from the University of Limerick, in 2004 and 2005, respectively, and the Ph.D. degree in biomedical engineering from the University of Galway, in 2011. From 2011 to 2022, he was with Valeo Vision Systems as a Vision Research Engineer focusing on image quality. His research interests include the relationship between blood pressure and cerebral blood flow in humans, high dynamic range imaging, LED flicker, topview harmonization algorithms, and the relationship between image quality and machine vision. In 2022, he joined the Department of Electrical and Electronic Engineering, University of Galway, as a Lecturer and a Researcher.

ANTHONY SCANLAN received the B.Sc. degree in experimental physics from the National University of Ireland Galway, Galway, Ireland, in 1998, and the M.Eng. and Ph.D. degrees in electronic engineering from the University of Limerick, Limerick, Ireland, in 2001 and 2005, respectively. He is currently a Senior Research Fellow with the Department of Electronic and Computer Engineering, University of Limerick, and has been the Principal Investigator on several research projects in the areas of signal processing and data converter design. His current research interests include artificial intelligence, computer vision, and industrial and environmental applications.

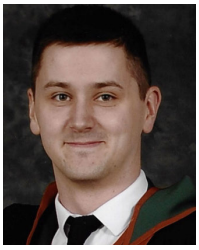

DARA MOLLOY received the B.Eng. degree (Hons.) from the University of Galway, in 2018, where he is currently pursuing the Ph.D. degree. He is a member of the Connaught Automotive Research (CAR) Group under the supervision of Prof. Martin Glavin and Prof. Edward Jones. His research interests include computer vision and sensor availability within an autonomous vehicle context.

ENDA WARD received the B.E. degree in electronic engineering from the University of Galway, in 1999, and the M.Eng.Sc. degree in electronic engineering, with a focus on biomedical electronics, in 2002. He is currently responsible for defining the camera product roadmap for surround and automated driving applications with Valeo. He has worked with key technology experts across the supply chain and within OEMs to define optimal system architectures. He lectured for a number of years in the areas of electronics and computing systems with Atlantic Technological University, Ireland. Later, he moved into industry, working in the biomedical space, and has spent the last 16 years in automotive ADAS design. He holds several patents in the area of automotive vision.

CIARÁN EISING (Senior Member, IEEE) received the B.E. and Ph.D. degrees from NUI Galway, in 20003 and 2010, respectively. Since 2009, he has been a Computer Vision Architect and a Senior Expert with Valeo. In 2020, he joined the University of Limerick as an Associate Professor of AI.